Title

Endothelial senescence is induced by phosphorylation and nuclear export of telomeric repeat binding factor 2–interacting protein

Permalink

https://escholarship.org/uc/item/61c0h5x7

Journal

JCI Insight, 4(9)

ISSN

2379-3708

Authors

Kotla, Sivareddy
Vu, Hang Thi
Ko, Kyung Ae
et al.

Publication Date

2019-05-02

DOI

10.1172/jci.insight.124867

JCI insight

Endothelial senescence is induced by phosphorylation and nuclear export of telomeric repeat binding factor 2–interacting protein

Sivareddy Kotla,[1] Hang Thi Vu,[1] Kyung Ae Ko,[1] Yin Wang,[1] Masaki Imanishi,[1] Kyung-Sun Heo,[1] Yuka Fujii,[1] Tamlyn N. Thomas,[1] Young Jin Gi,[1] Hira Mazhar,[1] Jesus Paez-Mayorga,[2,3] Ji-Hyun Shin,[1] Yunting Tao,[2] Carolyn J. Giancursio,[2] Jan L.M. Medina,[1] Jack Taunton,[4] Aldos J. Lusis,[5] John P. Cooke,[2] Keigi Fujiwara,[1] Nhat-Tu Le,[2] and Jun-ichi Abe[1]

[1]Department of Cardiology, The University of Texas MD Anderson Cancer Center, Houston, Texas, USA. [2]Center for Cardiovascular Regeneration, Department of Cardiovascular Sciences, Houston Methodist Research Institute, Houston, Texas, USA. [3]Tecnologico de Monterrey, Escuela de Medicina y Ciencias de la Salud, Monterrey, Nuevo Leon, Mexico. [4]Department of Cellular and Molecular Pharmacology, UCSF, San Francisco, California, USA. [5]Department of Human Genetics, David Geffen School of Medicine, UCLA, Los Angeles, California, USA.

The interplay among signaling events for endothelial cell (EC) senescence, apoptosis, and activation and how these pathological conditions promote atherosclerosis in the area exposed to disturbed flow (d-flow) in concert remain unclear. The aim of this study was to determine whether telomeric repeat-binding factor 2–interacting protein (TERF2IP), a member of the shelterin complex at the telomere, can regulate EC senescence, apoptosis, and activation simultaneously, and if so, by what molecular mechanisms. We found that d-flow induced p90RSK and TERF2IP interaction in a p90RSK kinase activity–dependent manner. An in vitro kinase assay revealed that p90RSK directly phosphorylated TERF2IP at the serine 205 (S205) residue, and d-flow increased TERF2IP S205 phosphorylation as well as EC senescence, apoptosis, and activation by activating p90RSK. TERF2IP phosphorylation was crucial for nuclear export of the TERF2IP-TRF2 complex, which led to EC activation by cytosolic TERF2IP-mediated NF-κB activation and also to senescence and apoptosis of ECs by depleting TRF2 from the nucleus. Lastly, using EC-specific TERF2IP-knockout (TERF2IP-KO) mice, we found that the depletion of TERF2IP inhibited d-flow–induced EC senescence, apoptosis, and activation, as well as atherosclerotic plaque formation. These findings demonstrate that TERF2IP is an important molecular switch that simultaneously accelerates EC senescence, apoptosis, and activation by S205 phosphorylation.

Authorship note: SK, HTV, KAK, YW, and MI contributed equally to this work. KF, NTL, and JA are co–senior authors.

Conflict of interest: JT is a cofounder of Principia Biopharma, which has licensed the p90RSK inhibitor FMK-MEA.

Submitted: September 14, 2018
Accepted: February 19, 2019
Published: April 4, 2019.

Reference information: *JCI Insight*. 2019;4(7):e124867. https://doi.org/10.1172/jci.insight.124867.

Introduction

Endothelial cell (EC) activation is characterized by the increased expression of adhesion molecules and chemokines that promote vascular inflammation (1). EC senescence is associated with EC activation, also known as senescence-associated secretory phenotype (SASP) (2). Telomere (TL) shortening contributes to EC senescence, which is associated with the development of atherosclerotic plaques (3, 4). It is well known that disturbed (as opposed to laminar) blood flow (d-flow) induces both EC activation and senescence (5, 6), but how these 2 pathological conditions are concomitantly upregulated by d-flow and subsequently lead to vascular plaque formation are poorly understood. The shelterin complex (TRF1, TRF2, TERF2IP, POT1, TPP1, and TIN2) of the mammalian TL (7) is known to maintain TL length. The complex appears to prevent TLs from shortening rather than to promote telomerase activity (8). In fact, telomerase activity is absent or very low in most adult tissues (7), and substantial evidence indicates that TL shortening, which is induced by depletion of the shelterin complex, is associated with cellular senescence (9, 10). However, whether the shelterin complex plays a role in atherogenesis is unclear. TERF2IP is a member of the shelterin complex of the mammalian TL and can bind both telomeric and nontelomeric chromatin (7), and it is involved in the protection of TLs (7). TERF2IP forms a complex with TRF2 (11), and the TERF2IP-TRF2 complex represses telomeric recombination, fragility, and shortening via its association with TLs (12).

Targeted TERF2IP deletion in stratified epithelia did not affect mouse viability, but it led to skin hyperpigmentation and shorter TLs in skin cells (13). The natural ends of chromosomes have a mechanism that prevents misdirected double-strand break repair, such as nonhomologous end joining (NHEJ) and homology-directed repair (HDR). These forms of repair can induce TL shortening and fragility, leading to DNA damage response and genome instability (14, 15). NHEJ causes dicentric chromosomes, which interfere with chromosome segregation during mitosis and can initiate the breakage-fusion-bridge cycle. HDR can result in unequal alterations among sister TLs and can be deleterious to cells that inherit a shortened TL (16). Both NHEJ and HDR can be repressed by TRF2 (15, 17). TERF2IP is required to repress HDR-mediated TL recombination (only in cells lacking Ku70) (12) but is dispensable for preventing NHEJ (12, 13). Therefore, it was suggested (7, 14) that deletion of TRF2 produces a more drastic phenotype (embryonic lethal) (18) than does deletion of TERF2IP (no effect on viability or fertility) in mice (12). It appears, however, that the role of TERF2IP in regulating TL length and senescence is context dependent. For example, Platt et al. report that TERF2IP significantly induced TL shortening by inhibiting histone-encoding genes and that the depletion of TERF2IP inhibited senescence in *Saccharomyces cerevisiae* (19). In contrast, Kabir et al. (14) report that, in immortalized human cell lines, the depletion of TERF2IP did not induce TL length changes and did not affect on the modification of telomeric histones and other TL defects (15). These authors suggest that TERF2IP conservation may reflect its transcriptional rather than telomeric function. Furthermore, the relationship between the TERF2IP-TRF2 complex and TL length can be intricate, and the role of the TERF2IP-TRF2 complex association with TLs may have other effects in addition to modulating TL length.

TERF2IP is not only found in TLs, but is also involved in NF-κB signaling in the cytosol, as it is required for the binding between NF-κB p65 and IκB kinases (20). TERF2IP stability in cells has been shown to depend on its association with TRF2, while TRF2 is stable without TERF2IP (12, 21). Therefore, Kabir et al. proposed that TERF2IP forms a stable complex with TRF2 inside cells. They further proposed that this complex shuttles between the nucleus and the cytosol (14). However, to our knowledge, this shuttling model has not been tested. Controversial data on the roles of TRF2 and TERF2IP in TL protection and DNA damage response have been reported (12, 13, 20). Martinez et al. (13) suggest that the amount of the TERF2IP-TRF2 complex that is bound vs. unbound depends on cell types, differentiation states, and experimental conditions and that deletion of TERF2IP vs. deletion of TRF2 produces different phenotypes in different cell types (7).

The aim of this study was to determine how the TERF2IP-TRF2 complex regulates both EC activation and senescence. Previously, we found a crucial role of p90RSK in regulating d-flow–induced EC inflammation and apoptosis (22). Therefore, we investigated the functional relationship between p90RSK and the TERF2IP-TRF2 complex under d-flow. We report here that d-flow induced p90RSK activation and upregulated TERF2IP serine 205 (S205) phosphorylation and that overexpression of kinase-dead p90RSK (KD-p90RSK) in ECs inhibited the TL shortening and NF-κB activation that were induced by d-flow. Mutation of the TERF2IP S205 phosphorylation site attenuated NF-κB activation in ECs by d-flow and also inhibited d-flow–elicited senescence and TL shortening. The depletion of TERF2IP inhibited d-flow–induced TRF2 nuclear export, and the TERF2IP S205A mutation attenuated the nuclear export of both TERF2IP and TRF2, suggesting that TERF2IP S205 phosphorylation has a crucial role in regulating nuclear export of both TERF2IP and TRF2.

The nuclear TERF2IP-TRF2 complex — in particular, nuclear TRF2 — protects TLs (23), while cytosolic TERF2IP plays a role in NF-κB activation (7, 14, 20). We found that the depletion of TERF2IP in ECs inhibited TRF2 nuclear export and protected TLs from d-flow–induced shortening. Lastly, we found that d-flow–induced atherosclerotic plaque formation seen in the mouse partial carotid ligation model was significantly inhibited in EC-specific TERF2IP-KO mice. Therefore, these results indicate that p90RSK mediates TL shortening and NF-κB activation by the following 2 molecular mechanisms: (a) TERF2IP and TRF2 nuclear export and (b) activation of NF-κB by TERF2IP S205 phosphorylation.

Results

Overexpression of KD-p90RSK and depletion of TERF2IP abolish d-flow–induced apoptosis and senescence in ECs. Previously, we reported that p90RSK activation has a crucial role in d-flow–induced EC apoptosis (22), but its role in senescence remains unclear. It has been reported that 2'-deoxyguanosine is the only one of the 4 native nucleotides of TLs that can be oxidized to form 8-hydroxy-2'-deoxyguanosine (8-oxo-dG), which is a marker of TL dysfunction and leads to increased genomic DNA damage and apoptosis (24). Therefore, we first tested whether d-flow causes 8-oxo-dG generation and TL shortening and then whether transduction of adenovirus containing KD-p90RSK (Ad-KD-p90RSK) could inhibit these d-flow–induced detrimental events in TLs. We found that d-flow indeed increased the level of 8-oxo-dG (Figure 1, A and B) and reduced TL lengths in ECs (Figure 1C). In addition, we found that these d-flow effects were significantly inhibited in Ad-KD-p90RSK–transduced ECs compared with Ad-LacZ–transduced control cells (Figure 1, A–C). We also compared d-flow–induced 8-oxo-dG induction in bovine aortic ECs and HUVECs in Figure 1, A and B, and found similar tendencies of KD-p90RSK–mediated inhibition of d-flow–induced 8-oxo-dG, also suggesting that HUVECs can recapitulate the d-flow–mediated biology in ECs isolated from the aorta.

Loss of protection by the shelterin complex accelerated oxidative damage in both TLs and genomic DNA. To examine the role of TERF2IP in d-flow–induced EC apoptosis and TL dysfunction, we depleted TERF2IP using siRNA in ECs, which were then exposed to d-flow. Interestingly, TERF2IP depletion inhibited d-flow–induced apoptosis (Figure 1, D–G) and TL dysfunction (Figure 1, H–J).

Depletion of TERF2IP inhibits d-flow–induced EC activation. To further understand the function of TERF2IP in ECs, we isolated total RNAs from human aortic ECs (HAECs) transfected with control or TERF2IP siRNA (Supplemental Figure 1A; supplemental material available online with this article; https://doi.org/10.1172/jci.insight.124867DS1) and performed transcriptional profiling. We performed an unpaired 1-way ANOVA with a statistical threshold of $P < 0.05$ and 1.5-fold change restriction to identify differentially expressed genes in control and TERF2IP siRNA–transfected cells that were not stimulated in any manner. We found that the top-ranked canonical pathway was neuroinflammation signaling. Six of 31 genes on the list belonged to this category, and all of them were expressed at lower levels in TERF2IP siRNA–transfected cells than in control cells (z-score, –2.449; $P = 8.52 \times 10^{-7}$) (Supplemental Figure 1B). Following Ingenuity Pathway Analysis network generation, function and disease gene enrichment was carried out; the activation of granulocytes was the highest scoring regulator effect network on the basis of the results of a right-tailed Fisher exact test (consistency core = 598.131; Supplemental Figure 1C), consistent with the previously suggested role of TERF2IP in granulocyte activation (25).

Next, we investigated the role of TERF2IP in d-flow–induced NF-κB activation and subsequent inflammatory gene expression. As shown in Supplemental Figure 1D, the depletion of TERF2IP completely inhibited d-flow–induced NF-κB activation, while TNF-α–induced NF-κB activation was only partially inhibited. We also found that d-flow–induced adhesion molecule expression was significantly decreased by the depletion of TERF2IP (Supplemental Figure 1E). These results indicate a key role for TERF2IP in EC activation, especially d-flow–induced EC activation.

p90RSK associates with the TERF2IP Myb domain and phosphorylates TERF2IP S205. Having found that p90RSK and TERF2IP are key molecules involved in d-flow–induced EC senescence and activation (Figure 1 and Supplemental Figure 1) and because both molecules can shuttle between the nucleus and the cytoplasm (14), we next investigated whether p90RSK can associate with TERF2IP. Using co-IP studies, we found that d-flow increased p90RSK association with TERF2IP (Figure 2A), which was dependent on p90RSK activation (Figure 2B). Using a mammalian 2-hybrid assay, we also found that p90RSK and TERF2IP were able to interact directly and that TNF-α stimulation increased this association (Figure 2C).

TERF2IP has 4 functional domains: a BRCA1 C-terminal domain, a Myb HTH motif, a coiled region, and a C-terminal protein interaction domain (23). The protein interaction domain is the binding site for TRF2, and the TERF2IP-TRF2 complex associates with TLs (11, 23, 26). The TERF2IP Myb domain may be involved in protein interactions (11). Indeed, using a mammalian 2-hybrid assay, we found that the Myb domain (aa 133–191) is a p90RSK binding site (Figure 2D). Overexpression of the TERF2IP-Myb fragment inhibited the association between p90RSK and TERF2IP (Figure 2E). Furthermore, this fragment

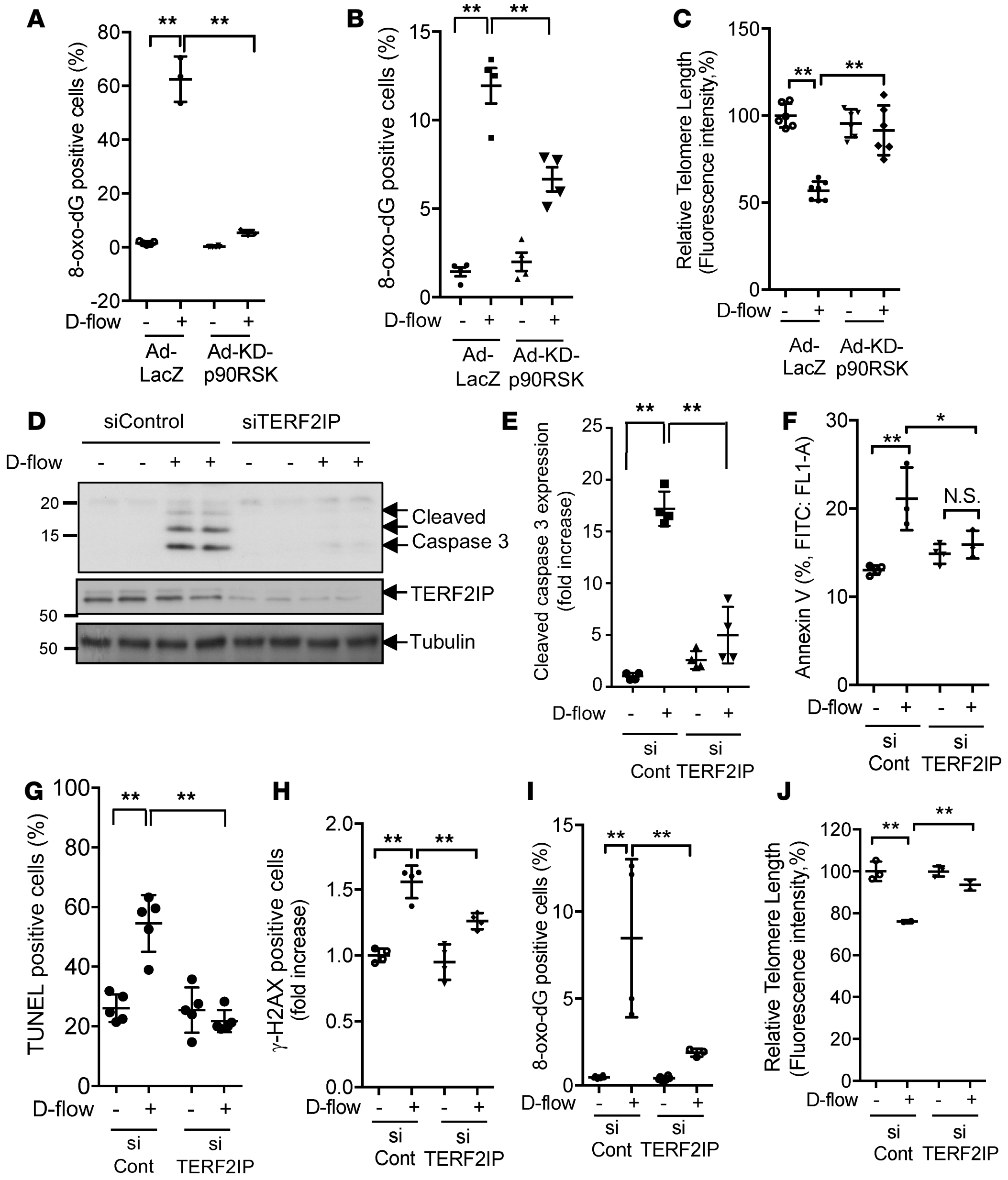

Figure 1. Expression of DNA damage response elements 8-oxo-2′-deoxyguanosine (8-oxo-dG) and γ-H2AX and apoptosis are upregulated by d-flow and inhibited by Ad-KD-p90RSK transduction and deletion of TERF2IP. (**A** and **B**) Flow cytometric analysis of 8-oxo-dG staining in bovine aortic endothelial cells (BAECs) or Human umblical vein endothelial cells (HUVEC) exposed to d-flow (8 hours). Graphs in **A** (BAEC) and **B** (HUVEC) show percentages of 8-oxo-dG–positive BAECs transduced with Ad-LacZ or Ad-KD-p90RSK and exposed to d-flow (8 hours). Error bars represent mean ± SD, *n* = 3–5, $^{**}P < 0.01$. (**C**) Flow cytometric analysis of TL shortening in HUVECs exposed to d-flow (24 hours). HUVECs were transduced by Ad-KD-p90RSK or Ad-LacZ, and TL length was assayed using the TL PNA kit/FITC for flow cytometry. The mean fluorescence intensity was used to estimate the relative TL length. Data were analyzed using FlowJo software. Error bars represent mean ± SD, *n* = 3. (**D**) HUVECs were transfected with TERF2IP or control siRNA and exposed to d-flow. Apoptosis was detected by Western blotting with anti–cleaved caspase 3. Images shown are representative of 3 independent experiments. (**E**) Quantification of the cleaved caspase 3 level is shown after normalization by total protein levels. Data represent mean ± SD, *n* = 3–4. (**F**) Percentage of annexin V–positive HUVECs exposed to d-flow (24 hours) after transfection with control siRNA (siCont) and siTERF2IP was determined by flow cytometry. Data represent mean ± SD, *n* = 3–4, $^{*}P < 0.05$, $^{**}P < 0.01$. (**G**–**J**) HUVECs were transfected with TERF2IP or control siRNA and then stimulated by d-flow or no flow for 24 hours (**G**, **H**, and **I**) or 8 hours (**J**), followed by TUNEL (**G**), γ-H2AX (**H**), or 8-oxo-dG (**I**) staining and TL length (**J**) measurements, as described above. Data represent the mean ± SD, *n* = 3–5, $^{*}P < 0.05$, $^{**}P < 0.01$. All statistical analyses in this figure were done by 1-way ANOVA followed by Bonferroni post hoc test.

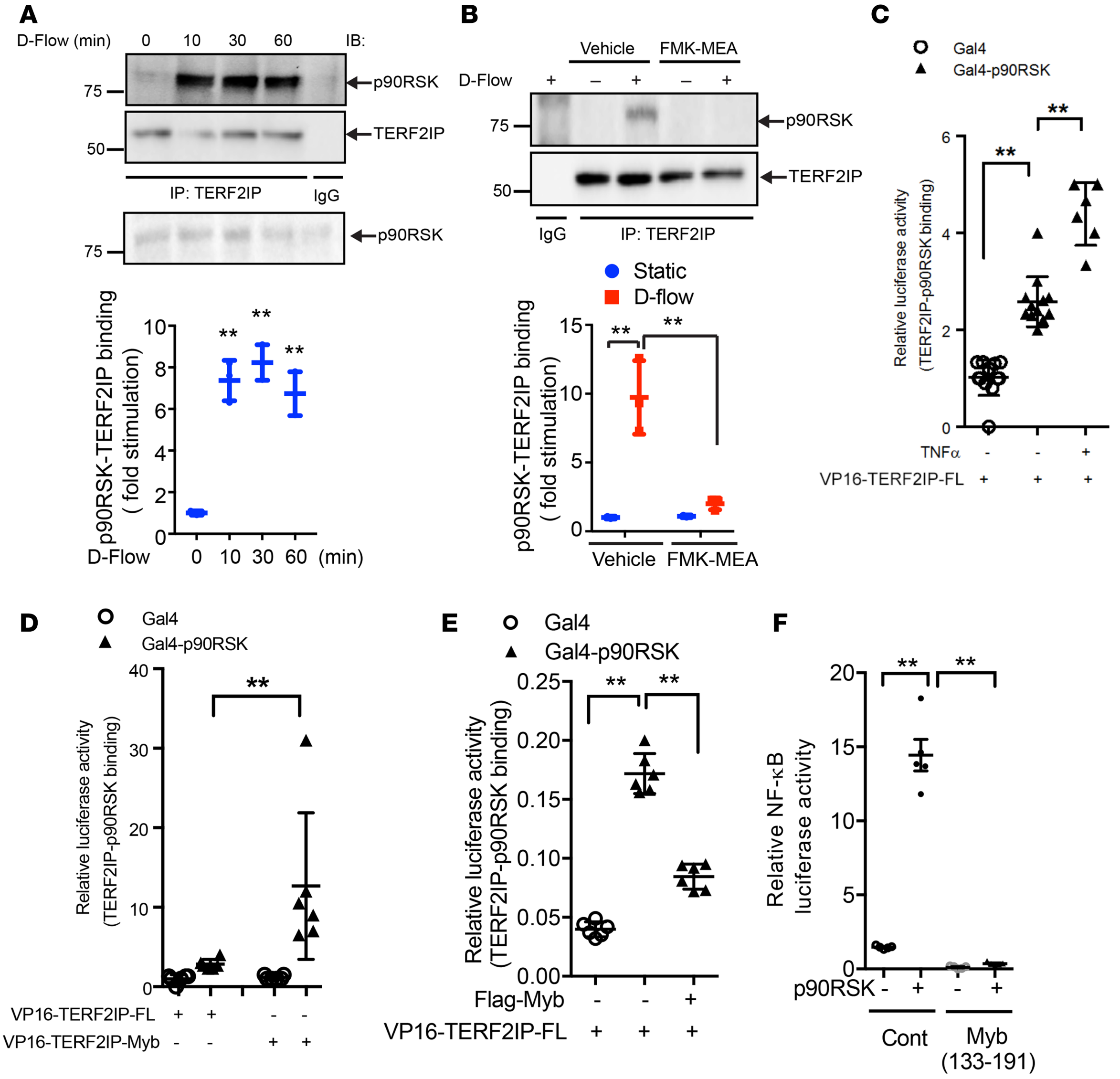

Figure 2. p90RSK associates with TERF2IP, and the p90RSK-TERF2IP Myb domain interaction has a critical role in regulating NF-κB activation. (**A**) HUVECs were exposed to d-flow for various lengths of time, as indicated, and cell lysates were immunoprecipitated with anti-TERF2IP or control IgG and immunoblotted with anti-p90RSK. Total cell lysates were immunoblotted with the indicated antibodies. Upper panel shows representative data from 3 independent experiments. Lower panel shows densitometric quantification of coimmunoprecipitated p90RSK with TERF2IP, which was normalized by total TERF2IP protein levels. Data represent mean ± SD, $n = 3$, $^{**}P < 0.01$. (**B**) HUVECs were pretreated with FMK-MEA and exposed to d-flow for 10 minutes. TERF2IP and p90RSK binding was detected as described in **A**. Data represent mean ± SD, $n = 3$, $^{**}P < 0.01$. Quantification analysis was also performed (lower panel). (**C**–**E**) HUVECs were transfected with plasmids containing Gal4-p90RSK WT, VP16-TERF2IP-FL (full length) (**C**), VP16-TERF2IP Myb fragment (**D**), Flag-tagged TEERF2IP Myb fragment (Flag-Myb) (**E**), or empty vector and Gal4-responsive luciferase reporter pG5-luc for 24 hours. Cells were stimulated with or without TNF for 2 hours (**C**), and luciferase activities were quantified. Data represent mean ± SD, $n = 6$–12. (**F**) HUVECs were transfected with plasmids containing WT p90RSK, VP16-TERF2IP Myb fragment, or VP16-empty vector (Cont) with the NF-κB activity reporter gene. After 24 hours of transfection, NF-κB activity was detected by a luciferase assay. Data represent mean ± SD, $n = 5$. All statistical analyses in this figure were done by 1-way ANOVA followed by Bonferroni post hoc test.

completely abolished p90RSK-induced NF-κB activation (Figure 2F). These results suggest that p90RSK and TERF2IP are capable of associating and that this binding is of functional importance.

Since p90RSK is a kinase, we also examined whether p90RSK can phosphorylate TERF2IP. Based on publicly available datasets for system-wide characterization of parallel quantitative proteomic and phospho-proteomic analyses (http://www.nextprot.org/db/entry/NX_Q9NYB0/sequence) and GPS 2.0 analysis (27), TERF2IP S205 is predicted to be a putative site for phosphorylation by p90RSK. We thus overexpressed a TERF2IP S205A or S205D mutant in ECs that were made to also overexpress p90RSK (to increase the basal level of p90RSK activity) (28). We found that the S205A mutation inhibited and the S205D mutation accelerated p90RSK-induced NF-κB activation (Figure 3, A and B, respectively). Using TERF2IP S205 phospho-specific rabbit polyclonal antibodies (Figure 3, C–E; made in-house), whose specificity was established by Western blotting (Figure 3C), we further showed that d-flow–induced endogenous TERF2IP S205 phosphorylation was inhibited by Ad-KD-p90RSK transduction (Figure 3, D and E). Furthermore, we performed an in vitro kinase assay by using recombinant p90RSK and immunoprecipitated TERF2IP and showed that p90RSK can directly phosphorylate TERF2IP S205 (Figure 3, F and G). Our findings suggest that p90RSK can both directly phosphorylate TERF2IP S205 and regulate its function.

TERF2IP S205 phosphorylation coinitiates EC senescence and activation. Having found the involvement of TERF2IP in cellular senescence (Figure 1), we next investigated whether TERF2IP S205 phosphorylation is involved in EC senescence. We first asked whether overexpression of p90RSK can induce EC senescence and whether reduced expression of TERF2IP can inhibit EC senescence induced by p90RSK overexpression. Transduction of Ad-WT-p90RSK significantly increased the number of senescence-associated β-gal$^+$ (SA–β-gal$^+$) ECs, and the depletion of TERF2IP significantly decreased such positive ECs (Figure 4, A–C).

Next, we transduced HAECs with Ad-TERF2IP S205A mutant or Ad-TERF2IP WT, exposed them to d-flow, and employed SA–β-gal staining to identify senescent cells. As shown in Figure 4D, d-flow increased the number of SA–β-gal$^+$ ECs in those transduced with Ad-TERF2IP WT, but this increase was completely abolished in Ad-TERF2IP S205A–transduced ECs. We confirmed equal expression levels of TERF2IP WT and TERF2IP S205A (Figure 4, D and E). We also found that d-flow–induced apoptosis, as detected by both annexin V expression and TUNEL staining in Ad-TERF2IP WT, S205A, and S205D-transduced ECs, was significantly reduced in TERF2IP S205A–transduced cells (Figure 4, F, H, and I) and accelerated in S205D-transduced cells (Figure 4G). These results suggest a crucial role for TERF2IP S205 phosphorylation in EC senescence and apoptosis induced by p90RSK activation and d-flow.

Next, we evaluated the role of TERF2IP in regulating NF-κB and subsequent inflammatory genes expression. We found that the depletion of TERF2IP in HAECs or HUVECs significantly inhibited d-flow–induced expression of adhesion molecules (Supplemental Figure 1E and Supplemental Figure 2A). We also found the crucial role of TERF2IP in d-flow–induced expression of adhesion molecules in HUVECs (Supplemental Figure 2A). To determine whether TERF2IP S205 phosphorylation is also involved in NF-κB activation by TNF-α, we transfected HUVECs with TERF2IP S205A or TERF2IP WT, exposed the cells to TNF-α (Supplemental Figure 2B) or d-flow (Supplemental Figure 2C), and examined NF-κB activation as well as expression of inflammatory genes regulated by NF-κB. NF-κB activation by TNF-α or by d-flow was inhibited in cells expressing TERF2IP S205A compared with cells expressing WT TERF2IP (Supplemental Figure 2, B and C), supporting the key role of TERF2IP S205 phosphorylation in EC activation. Taken together, these results suggest the crucial role of TERF2IP S205 phosphorylation in upregulating EC senescence, apoptosis, and activation.

TERF2IP S205 phosphorylation is required for d-flow–induced TERF2IP nuclear export. Next, we investigated the role of TERF2IP S205 phosphorylation in regulating TERF2IP nuclear export. We found that D-flow significantly increased endogenous TERF2IP nuclear export (Figure 5, A and B). It has been reported that TERF2IP is an IKK binding protein, and activated IKKs localize in the perinuclear area, especially around the centrosome (29). Therefore, to associate with IKKs in the cytosol, it is possible that cytosolic TERF2IP has a perinuclear location. To detect whether TERF2IP S205 phosphorylation played a role in TERF2IP nuclear export, we overexpressed the Flag-tagged WT or S205A mutant of TERF2IP in ECs and exposed them to d-flow. As shown in Figure 5C, both TERF2IP WT and S205A mutant localized in the nucleus under the static condition. After d-flow, however, Flag-tagged TERF2IP WT was detected in the cytoplasm, while TERF2IP S205A stayed in the nucleus, indicating that TERF2IP S205 phosphorylation is necessary for d-flow–induced TERF2IP nuclear export (Figure 5, C and D).

We next examined endothelial TERF2IP expression and localization in vivo and found that TERF2IP is expressed in the d-flow area at the aortic arch, especially in the cytosol. In contrast, TERF2IP expression in the laminar flow (l-flow) area was much lower (Figure 6, A and B). Previously, we reported that both p90RSK phosphorylation and signaling were increased in the d-flow area (22). Therefore, we evaluated endothelial TERF2IP S205 phosphorylation in vivo by using en face confocal microscopy; we found that the anti-phospho–specific TERF2IP S205 staining intensity was much higher in the d-flow area than that in the l-flow area (Figure 6, C and D).

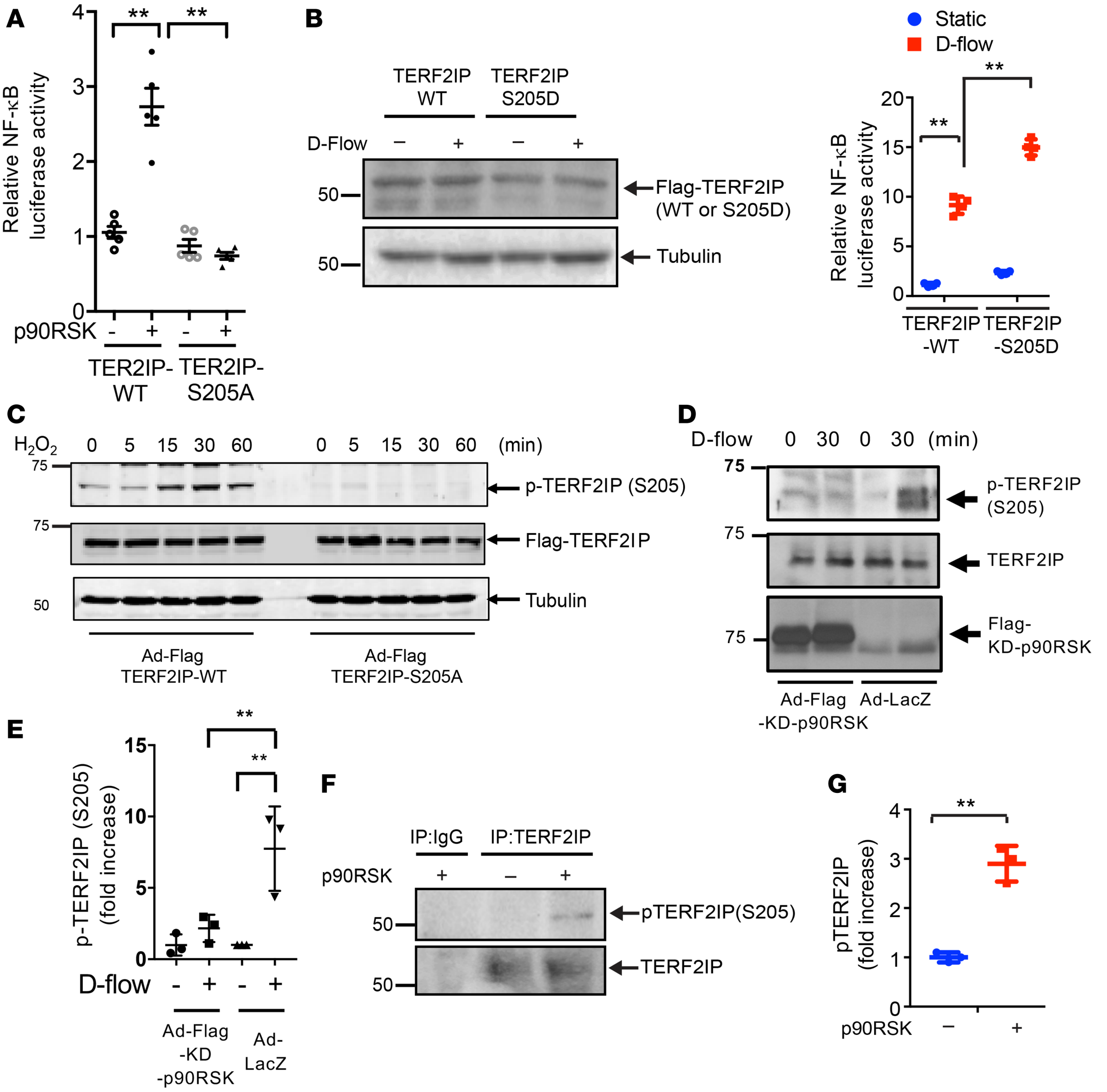

Figure 3. p90RSK phosphorylates TERF2IP S205 and increases NF-κB activation. (**A** and **B**) After 24 hours of transfection of NF-κB activity reporter gene and either TERF2IP WT or an S205A mutant treated with and without p90RSK or LacZ as a control (**A**), or S205D (**B**) mutant with and without d-flow, NF-κB activity was detected by luciferase assay. Expression of TERF2IP WT, TERF2IP-S205D, and tubulin was determined by Western blotting and with and without d-flow (**B**, left panel). Data represent mean ± SD, $n = 5$, $^{**}P < 0.01$. (**C** and **D**) Protein expression of p-TERF2IP-S205, TERF2IP, and tubulin (loading control) (**C**) and Flag-KD-p90RSK (**D**) in lysates of HUVECs transduced with Ad-Flag-TERF2IP WT or -S205A mutant (**C**) or KD-p90RSK (**D**) and exposed to H_2O_2 (200 μM) (**C**) or d-flow (**D**) was assessed by Western blotting. Graph (**E**) shows densitometric quantification of phosphorylated TERF2IP-S205, which was normalized by total TERF2IP protein levels. Shown are representative data from 3 independent experiments. Data represent mean ± SD, $n = 3$–5, $^{**}P < 0.01$. (**F**) An in vitro kinase assay was performed using immunoprecipitated TERF2IP in the absence or presence of recombinant p90RSK followed by immunoblotting with anti–p-TERF2IP (S205) (upper panel). The same amount of recombinant TERF2IP was immunoprecipitated by anti-TERF2IP, as indicated by anti-TERF2IP immunoblotting (lower panel). (**G**) Graph shows densitometric quantification of phosphorylated TERF2IP-S205, which was normalized by total TERF2IP protein levels. Data represent mean ± SD, $n = 3$, $^{**}P < 0.01$. Statistical analyses in **A**–**F** were done by 1-way ANOVA followed by Bonferroni post hoc test, and statistical analysis in **G** was performed by unpaired 2-tailed *t* test.

D-flow induces nuclear export of the TERF2IP-TRF2 complex. The complex formation between TERF2IP and TRF2 and its critical role in regulating cellular senescence have been reported (14). We therefore investigated how d-flow regulates TERF2IP and TRF2 nuclear exports. We also found an association between TERF2IP and TRF2, but this interaction was significantly inhibited after 60 minutes of d-flow (Figure 7, A and B). It has been reported that cytoplasmic TERF2IP is not associated with TRF2 (21). This observation may be supportive of our result that TERF2IP is exported from the nucleus in ECs under d-flow. The crucial role of TRF2 in TERF2IP protein stability has also been reported (11, 30). In fact, the decrease of TERF2IP expression and NF-κB activation that we observed after siTRF2 transfection (Figure 7, C and D) supports this notion. Although the role

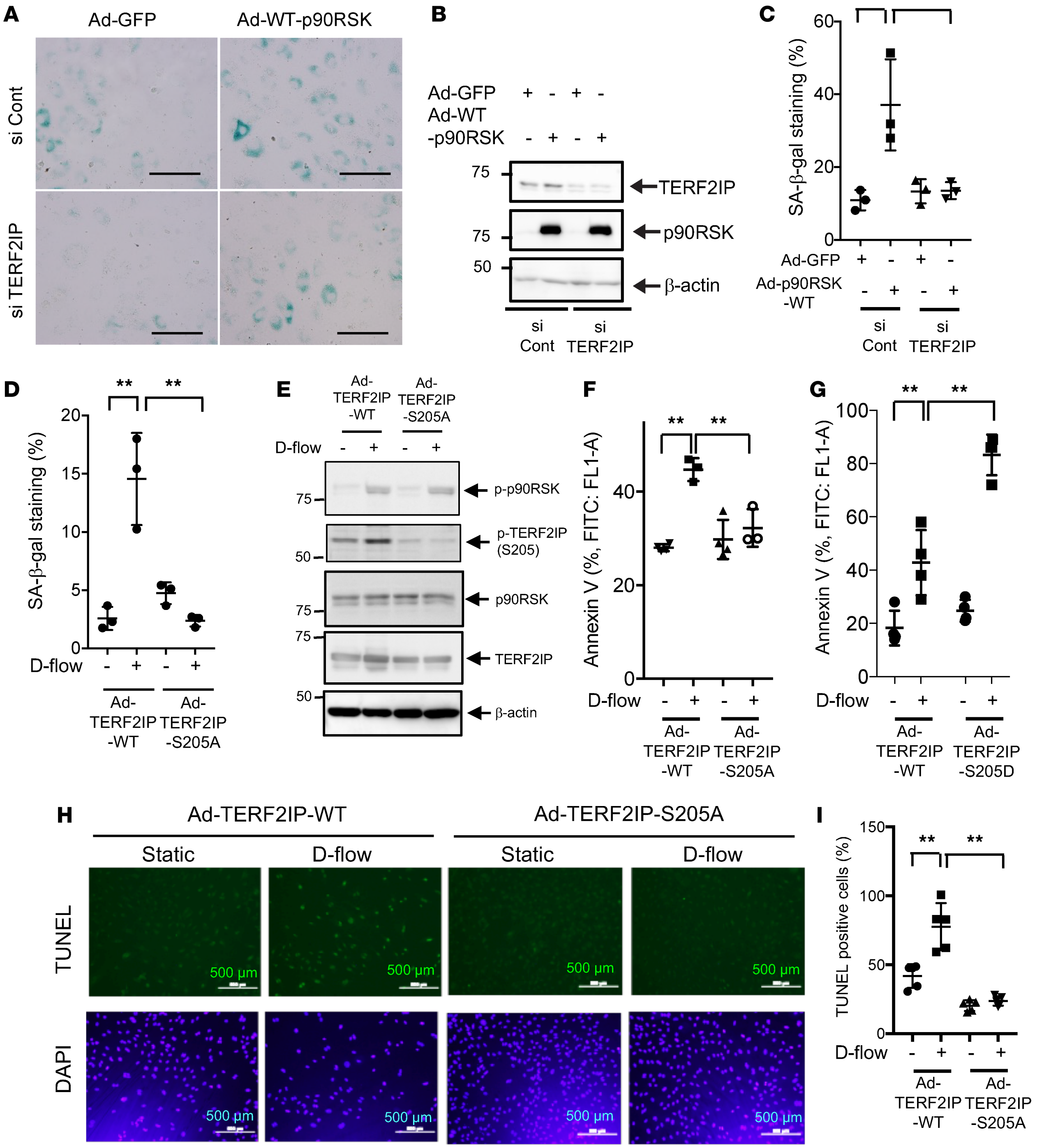

Figure 4. TERF2IP S205 phosphorylation plays a crucial role in EC senescence. (**A**–**C**) Human aortic endothelial cells (HAECs) were incubated with TERF2IP or control siRNA for 48 hours and transduced by adenovirus containing p90RSK (Ad-WT-p90RSK) or GFP (Ad-GFP) for 24 hours. (**A**) EC senescence was evaluated by SA-β-gal staining. Scale bars: 100 μm. (**B**) Reduced expression of TERF2IP after siRNA transfection and expression levels of exogenous p90RSK were detected by Western blotting. (**C**) The percentages of cells positive for SA-β-gal staining are shown. More than 200 cells/sample were counted. The data represent mean ± SD, *n* = 3. (**D**–**F**) HUVECs were transduced by Ad-TERF2IP WT or Ad-TERF2IP S205A mutant for 24 hours and then exposed to d-flow for 16 hours. (**D**) Cell senescence was evaluated by SA-β-gal staining and quantified as in **C**. The data represent mean ± SD, *n* = 3. (**E**) Expression of TERF2IP WT and S205A and β-actin as determined by Western blotting. (**F**) Graph shows fold increase of annexin V–positive cells analyzed by flow cytometry among Ad-TERF2IP WT–transduced HUVECs exposed to d-flow (24 hours) compared with similarly treated cells expressing the Ad-TERF2IP S205A mutant. The data represent mean ± SD, *n* = 3–5. (**G**) Annexin V–positive cells among Ad-TERF2IP WT– and -S205D–transfected HUVECs were detected. The data represent mean ± SD, *n* = 3–5. (**H** and **I**) HUVECs were transduced with Ad-TERF2IP WT or Ad-TERF2IP S205A for 18 hours and then stimulated by d-flow or no flow for 36 hours, followed by TUNEL staining. DAPI staining was used to identify nuclei. Quantification of apoptosis is shown as the percentage of TUNEL-positive cells (**I**). More than 200 cells were counted for each category. Data represent mean ± SD, *n* = 5, $^{**}P < 0.01$, $^{*}P < 0.05$. All statistical analyses in this figure were done by 1-way ANOVA followed by Bonferroni post hoc test.

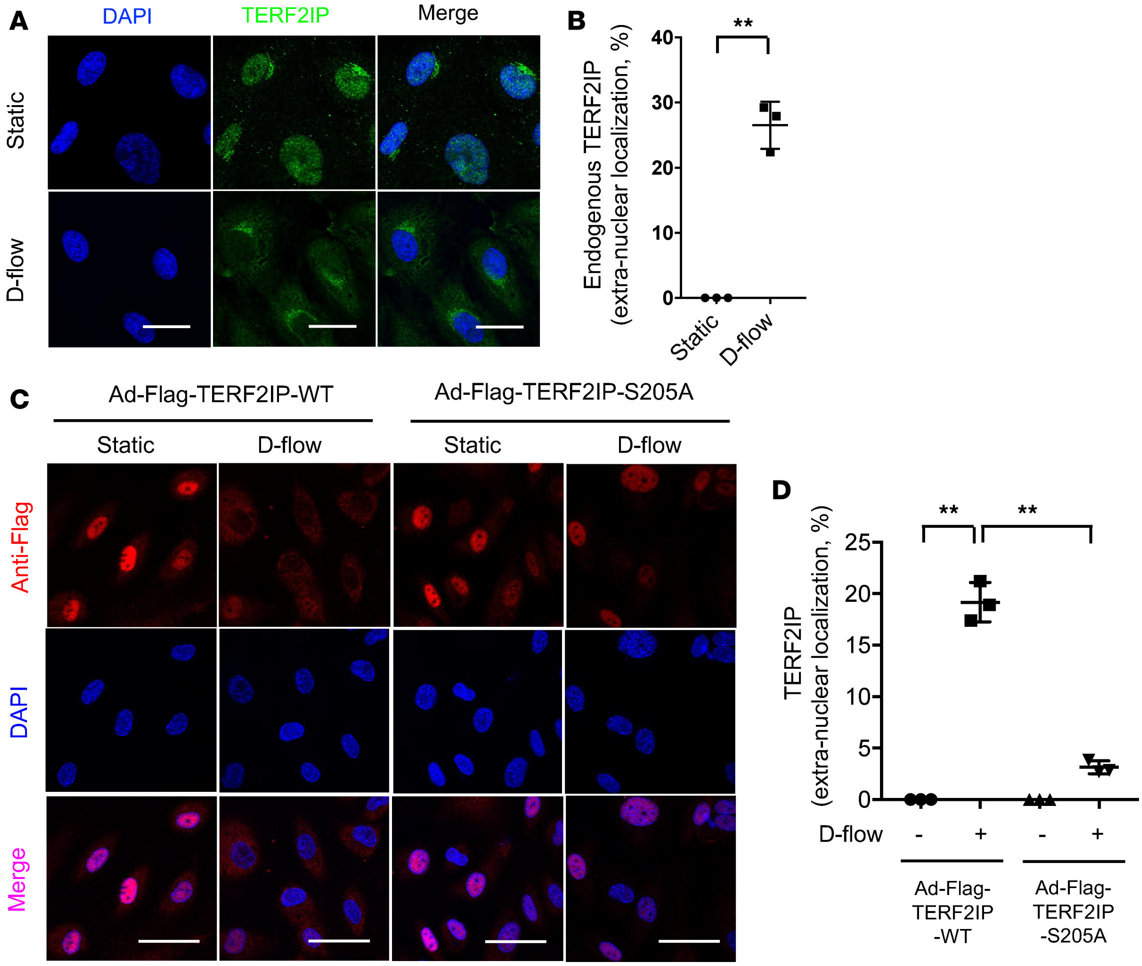

Figure 5. TERF2IP S205 phosphorylation is crucial for d-flow–induced nuclear export of TERF2IP. (**A**) HUVECs were exposed to d-flow for 4 hours and stained with anti-TERF2IP and DAPI. Single confocal optical sections roughly 5 μm above the substrate plane were captured using an Olympus confocal microscope (FV1200 MPE) with a 60× objective lens (NA 1.35na Oil). Faint but detectable anti-TERF2IP staining in the cytoplasm can be detected in cells exposed to d-flow. Scale bars: 20 μm. The percentages of cells with cytoplasmic staining were calculated and presented in **B**. More than 200 cells from 3 independent experiments were scored for each group. Data are presented as mean ± SD $^{**}P < 0.01$ by unpaired 2-tailed *t* test. Scale bars: 20 μm. (**C**) HUVECs were transduced with adenovirus containing Flag-TERF2IP (Ad-Flag-TERF2IP WT) or Flag-TERF2IP S205A and stimulated with or without d-flow for 3 hours. After fixation, cells were then stained by anti-Flag and DAPI and imaged as in **A**. Note that a portion of exogenously expressed WT TERF2IP, which was localized in the nucleus in static cells, translocated into the cytoplasm only when cells were exposed to d-flow. This d-flow–dependent TERF2IP extranuclearization was not observed in cells expressing the S205A mutant. The percentages of cells with cytoplasmic staining were quantified by counting >200 cells/group from 3 independent experiments and are shown in **D**. Data are presented as mean ± SD $^{**}P < 0.01$ by 1-way ANOVA followed by Bonferroni post hoc test.

of TERF2IP in regulating TL length is somewhat controversial, TRF2's role in TL length regulation and end protection is well established; the depletion of TRF2 causes massive NHEJ pathway–mediated end-to-end chromosome fusion and severe DNA damage (17, 31). In ECs, we also found that TRF2 depletion induced apoptosis and enhanced d-flow–induced apoptosis (Figure 7E). Furthermore, TRF2 depletion caused a significant decrease in TL length (Figure 7F). Taken together, these data suggest the potential role of nuclear export of the TERF2IP-TRF2 complex and subsequent loss of nuclear TRF2 in engendering TL shortening and apoptosis.

Shuttling of the TERF2IP-TRF2 complex between the nucleus and the cytosol has been proposed (14), but to our knowledge, it has not been tested. Although TERF2IP and TRF2 form a complex, each molecule plays a distinct role in regulating TL length and apoptosis. Therefore, we investigated TRF2 intracellular localization in ECs after depleting TERF2IP or overexpressing the TERF2IP S205A mutant. In control cells, we found that both TERF2IP (Figure 5, A and B) and TRF2 (Figure 7, G and H) translocated to the cytosol from the nucleus when ECs were exposed to d-flow, but TRF2 nuclear export was completely inhibited in TERF2IP-depleted cells (Figure 7, G and H). In addition, overexpression of the

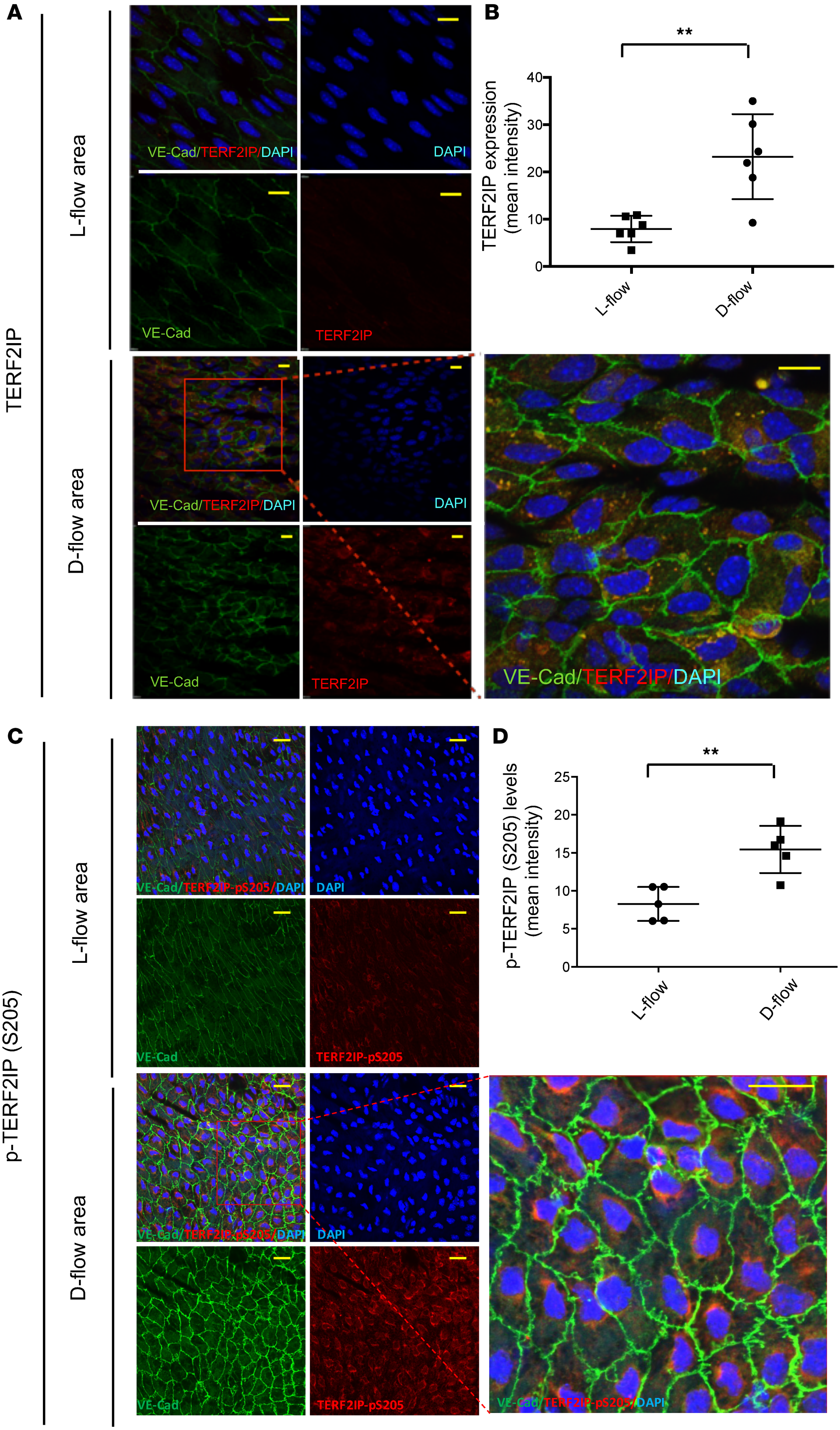

Figure 6. TERF2IP expression and S205 phosphorylation increase in the d-flow area in vivo. (**A** and **C**) En face preparations of the aortic arch of 7-week-old WT C57BL/6 mice were triple-stained with anti–vascular endothelial cadherin (as an EC marker), anti-TERF2IP (**A**), anti–p-TERF2IP S205 (**C**), and DAPI. Scale bars: 20 μm. Representative images from 3 independent experiments are shown. (**B** and **D**) The histograms show the increased mean intensity of anti-TERF2IP (**B**) and anti–p-TERF2IP S205 (**D**) staining in the d-flow area. Data are presented as mean ± SD $^{**}P < 0.01$ by unpaired 2-tailed *t* test.

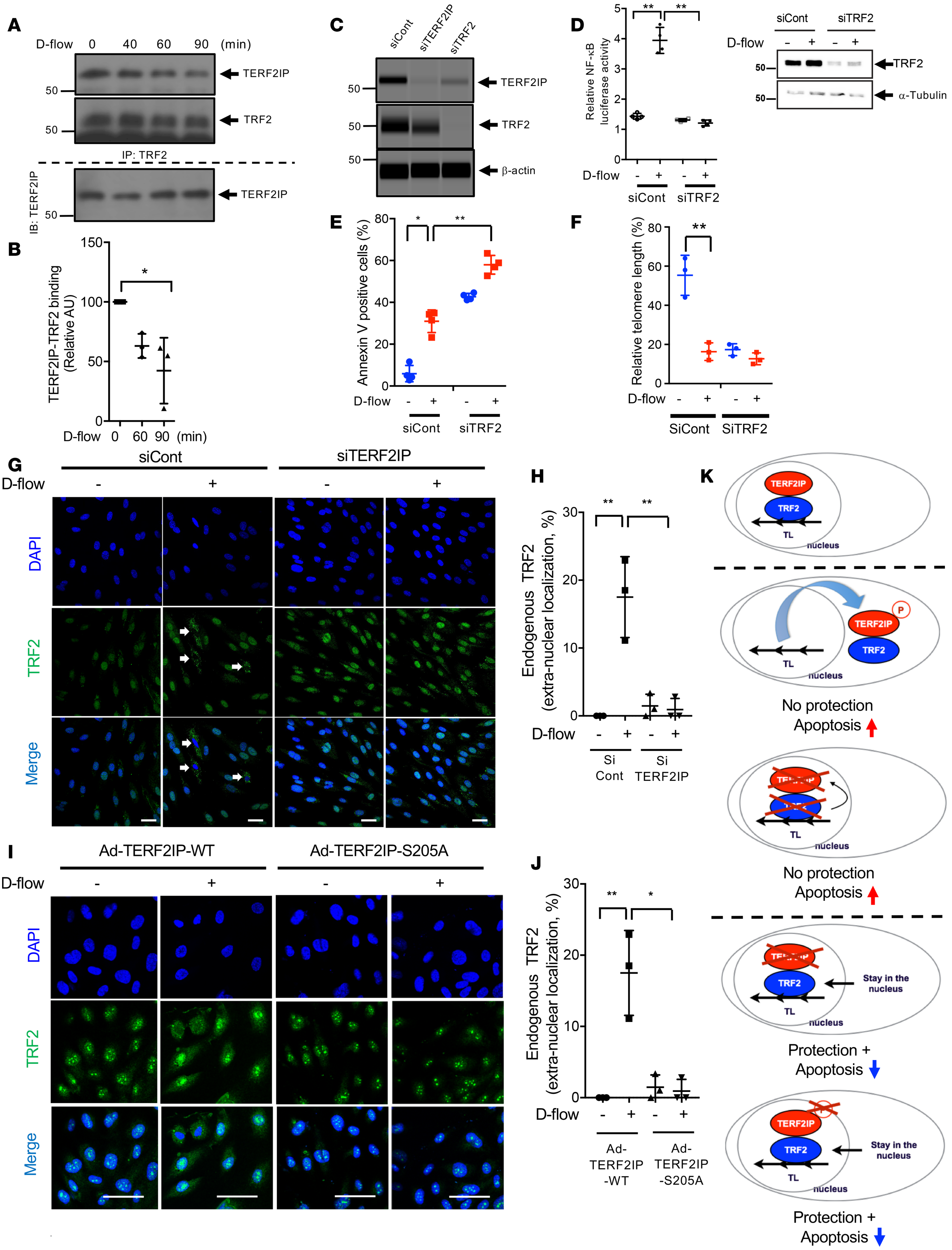
A
D-flow 0 40 60 90 (min)
50
TERF2IP
50
TRF2
IP: TRF2
IB: TERF2IP
50
TERF2IP
B
TERF2IP-TRF2 binding (Relative AU)
150
100
50
0
*
D-flow 0 60 90 (min)
C
siCont
siTERF2IP
siTRF2
50
TERF2IP
50
TRF2
50
β-actin
D
Relative NF-κB luciferase activity
5
4
3
2
1
0
**
**
D-flow - + - +
siCont siTRF2
siCont siTRF2
D-flow - + - +
50
TRF2
50
α-Tubulin
E
Annexin V positive cells (%)
80
60
40
20
0
*
**
D-flow - + - +
siCont siTRF2
F
Relative telomere length (%)
80
60
40
20
0
**
D-flow - + - +
SiCont SiTRF2
G
siCont
siTERF2IP
D-flow - + - +
DAPI
TRF2
Merge
H
Endogenous TRF2 (extra-nuclear localization, %)
30
20
10
0
**
**
D-flow - + - +
Si Cont
Si TERF2IP
I
Ad-TERF2IP-WT
Ad-TERF2IP-S205A
D-flow - + - +
DAPI
TRF2
Merge
J
Endogenous TRF2 (extra-nuclear localization, %)
30
20
10
0
**
*
D-flow - + - +
Ad-TERF2IP-WT
Ad-TERF2IP-S205A
K
TERF2IP
TRF2
TL
nucleus
P
TERF2IP
TRF2
TL
nucleus
No protection
Apoptosis ↑
TERF2IP
TRF2
TL
nucleus
No protection
Apoptosis ↑
TERF2IP
TRF2
Stay in the nucleus
TL
nucleus
Protection +
Apoptosis ↓
TERF2IP
TRF2
Stay in the nucleus
TL
nucleus
Protection +
Apoptosis ↓

Figure 7. TERF2IP S205 phosphorylation is required for nuclear export of the TERF2IP-TRF2 complex. (**A**) HUVECs were exposed to d-flow for 0–90 min.; binding between TERF2IP and TRF2 was analyzed by co-IP with anti-TRF2, followed by Western blotting with anti-TERF2IP. Total TERF2IP in each sample is shown (bottom). Representative images from 3 independent experiments are shown. (**B**) Quantification of TERF2IP-TRF2 binding is shown after normalization to levels at 0 min. *n* = 3–4. (**C**) Reduced expression of TERF2IP and TRF2 following transfection with TERF2IP and TRF2 siRNA was detected by Western blotting. Representative images from 3 independent experiments are shown. (**D**) After 24 hours of transfection with the NF-κB reporter gene together with control or TRF2 siRNA, HUVECs were exposed to d-flow for 24 hours, and NF-κB activity was measured by the luciferase assay (left). TRF2 and tubulin expression were detected by Western blotting (right). *n* = 4. (**E** and **F**) FITC annexin V–positive cells (**E**) and TL length (**F**) in HUVECs transfected with TRF2 or control siRNA were determined after 24 hours of d-flow or static culture. (**G** and **H**) After 48 hours of TERF2IP or control siRNA transfection, HUVECs were exposed to d-flow for 4 hours and stained with anti-TRF2 and DAPI. (**G**) In ECs exposed to d-flow, anti-TRF2 staining became detectable in control cells but not siTERF2IP-treated cells. Scale bars: 50 μm. (**H**) Extranuclear localization of TRF2 (%) was calculated by counting more than 200 cells/sample for each group. *n* = 3. (**I**) After transduction with Ad-TERF2IP WT and -S205A, HUVECs were exposed to d-flow for 4 hours and stained with anti-TRF2 and DAPI. Note d-flow–induced translocation of TRF2 into the cytoplasm. Scale bars: 50 μm. (**J**) Extranuclear localization of TRF2 (%) was calculated by counting more than 200 cells/sample for each group. *n* = 3. Data represent mean of percentages ± SD. $^{**}P < 0.01$, $^{*}P < 0.05$. All statistical analyses were done by 1-way ANOVA followed by Bonferroni post hoc test. (**K**) Proposed scheme of the TERF2IP-TRF2 complex nuclear export. Nuclear TRF2 is critical for protecting TLs from shortening. TERF2IP can deliver TRF2 to the cytoplasm. TERF2IP S205 phosphorylation causes the TERF2IP-TRF2 complex to move out of the nucleus and induces TL shortening and subsequent apoptosis (middle 2 panels). Both depletion of TERF2IP and inhibition of TERF2IP S205 phosphorylation prevent TRF2 nuclear export and protect TLs (bottom 2 panels).

TERF2IP S205A mutant, which could not translocate to the cytosol (Figure 5, C and D), inhibited TRF2 nuclear export after d-flow (Figure 7, I and J). Taken together, these results show that d-flow–induced TERF2IP S205 phosphorylation is essential for both TERF2IP and TRF2 nuclear export. It is possible that TRF2 extranuclear translocation is achieved by a piggy-back mechanism with TERF2IP (Figure 7K). Since TRF2 is indispensable for protecting TL ends and inhibiting apoptosis, our data suggest that depletion of TERF2IP or inhibition of TERF2IP S205 phosphorylation protects TLs and suppresses d-flow–induced apoptosis by inhibiting TRF2 nuclear export (Figure 7K).

TERF2IP simultaneously regulates EC activation and senescence and subsequent d-flow–induced atherosclerotic plaque formation. To specifically study the role of TERF2IP in ECs in vivo, we generated EC-specific heterozygous and homozygous Terf2ip-KO mice using mice that expressed Cre-recombinase under the regulation of the vascular endothelial-cadherin (VE-Cad) promoter (22) (VE-Cad-Cre Tg [Terf2ip$^{fl/+}$ or Terf2ip$^{fl/fl}$]; herein referred to as Terf2ip^{het}–EC-specific knockout (EKO) or Terf2ip^{homo}-EKO, respectively). As controls, we used nontransgenic littermates (nonlittermate control [NLC]: VE-Cad-Cre$^{+/–}$ Tg [Terf2ip$^{+/+}$] or VE-Cad-Cre$^{–/–}$ Tg [Terf2ip$^{fl/+}$ or Terf2ip$^{fl/fl}$]). First, we established primary cultures of mouse lung ECs (MLECs) and mouse aortic ECs (MAoECs) from Terf2ip^{homo}-EKO mice and exposed them to d-flow. EC activation (NF-κB activation and expression of VCAM-1, and intracellular adhesion molecule-1 [ICAM-1]), EC senescence (TL shortening), and apoptosis (annexin V) induced by d-flow (MLECs, Figure 8, A–C) or by overexpression of p90RSK (Figure 8, D–F, MLECs; Supplemental Figure 3, MAoECs) were all attenuated in ECs isolated from Terf2ip^{homo}-EKO mice.

To determine the role of TERF2IP in EC activation and apoptosis in vivo, we isolated aortas from 7-week-old male *Ldlr* (C57BL/6) and *Terf2ip*^{het}-EKO/*Ldlr* mice that had been fed normal chow for 2 weeks. En face preparations of aortas were immunostained with anti–VE-cadherin and anti–VCAM-1 or anti–cleaved caspase 3. DAPI was used to label nuclei. VCAM-1 expression and cleaved caspase 3 signals were significantly higher in the d-flow area for *Ldlr* mice than for *Terf2ip*^{het}-EKO/*Ldlr* mice (Figure 9, A–D). These results suggest that EC TERF2IP has a crucial role in both d-flow–induced activation and apoptosis in vivo.

Lastly, to explore the role of endothelial TERF2IP in d-flow–induced atherogenesis, we employed partial ligation of the left carotid artery in NLC/*Ldlr*$^{–/–}$ and *Terf2ip*^{het}-EKO/*Ldlr*$^{–/–}$ mice, which were then fed a high-fat diet. We chose to use *Terf2ip*^{het}-EKO rather than *Terf2ip*^{homo}-EKO because it would be rare that complete depletion of TERF2IP in mice would occur in nature. The partial left carotid artery ligation (PLCL) mouse model has been used to experimentally generate an area of d-flow where atherogenic responses are induced in a short period of time (32–34). We found no notable difference in cholesterol levels among these mice after partial ligation (Supplemental Figure 4). Plaque formation in *Terf2ip*^{het}-EKO/*Ldlr*$^{–/–}$ mice was suppressed compared with that in NLC/*Ldlr*$^{–/–}$ mice (Figure 9, E–G). These results demonstrate that endothelial TERF2IP has a atherogenic role.

We also performed PLCL in *Terf2ip*^{homo}-EKO/*Ldlr* mice and found no difference in lesion sizes between *Terf2ip*^{homo}-EKO/*Ldlr* and control mice, and the homozygosity did not show further atheroprotective effects compared with those shown in *Terf2ip*^{het}-EKO/*Ldlr* mice (Figure 9H). It has been reported

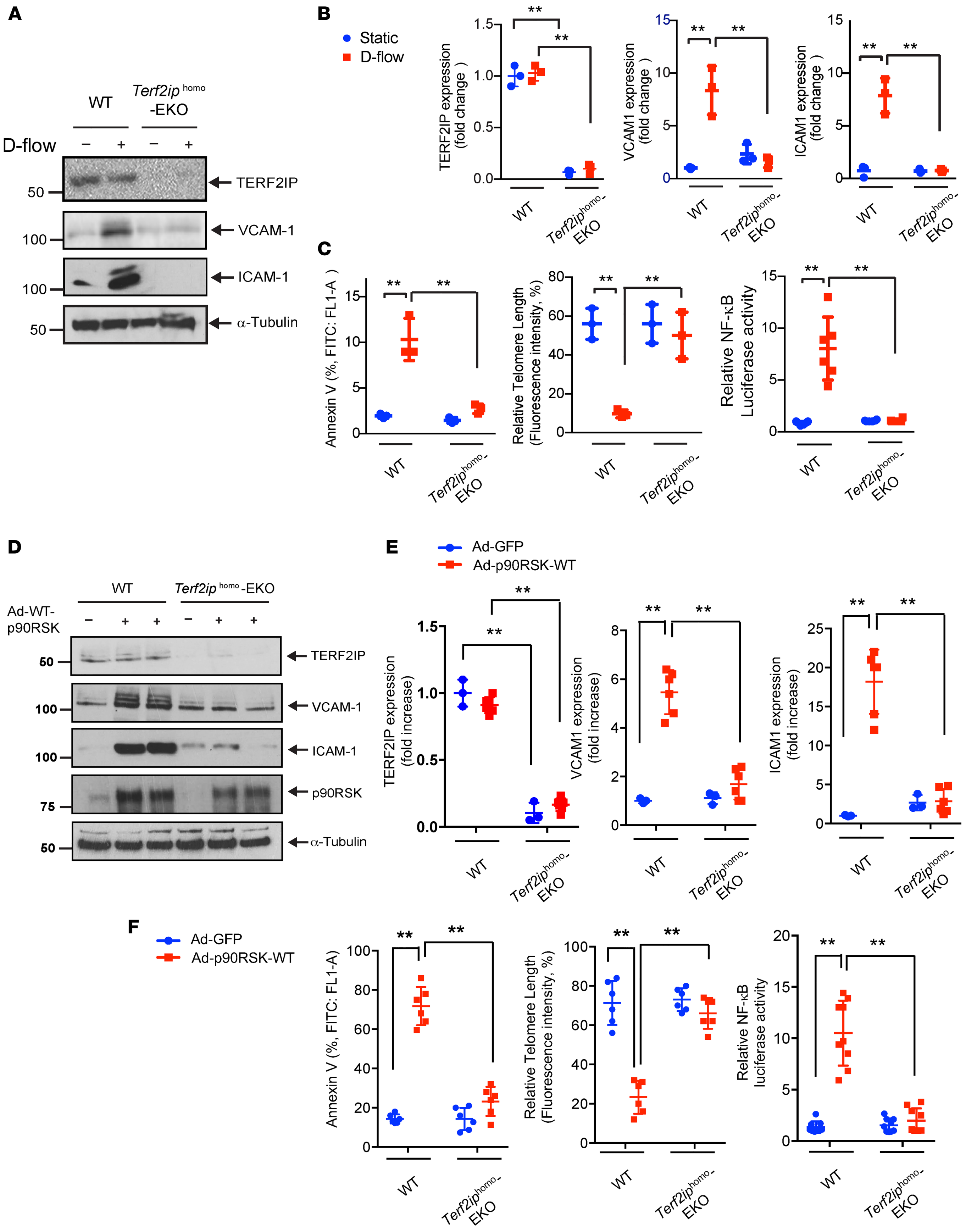
A
WT
Terf2ip homo -EKO
D-flow
− + − +
50
100
100
50
TERF2IP
VCAM-1
ICAM-1
α-Tubulin
B
Static
D-flow
TERF2IP expression (fold change)
VCAM1 expression (fold change)
ICAM1 expression (fold change)
**
WT
Terf2ip homo-EKO
C
Annexin V (%, FITC: FL1-A)
Relative Telomere Length (Fluorescence intensity, %)
Relative NF-κB Luciferase activity
D
WT
Terf2ip homo -EKO
Ad-WT-p90RSK
− + + − + +
50
100
100
75
50
TERF2IP
VCAM-1
ICAM-1
p90RSK
α-Tubulin
E
Ad-GFP
Ad-p90RSK-WT
TERF2IP expression (fold increase)
VCAM1 expression (fold increase)
ICAM1 expression (fold increase)
F
Ad-GFP
Ad-p90RSK-WT
Annexin V (%, FITC: FL1-A)
Relative Telomere Length (Fluorescence intensity, %)
Relative NF-κB luciferase activity

Figure 8. Depletion of TERF2IP inhibits EC senescence and activation in vitro. (**A**–**C**) Mouse lung endothelial cells (MLECs) were isolated from WT or *Terf2ip*^{homo}–EC-specific KO (EKO) mice. After treatment of cells with d-flow or static conditions for 12 hours, protein expression was analyzed by Western blotting using specific antibodies as indicated **A**, and the level of each protein expression under different conditions was quantified **B**. Data represent mean ± SD, $n = 3$. (**C**) Cell apoptosis, TL length, and NF-κB activity were quantified. Data represent mean ± SD, $n = 3–6$, $^{**}P < 0.01$. (**D**) MLECs were isolated from WT or *Terf2ip*^{homo}–EKO (TERF2IP-EKO) mice. After transduction of Ad-p90RSK WT or Ad-GFP as a control for 12 hours, Western blotting was performed using specific antibodies as indicated. (**E**) Graphs represent densitometry data of immunoblots from 3 independent experiments. Data represent mean ± SD. (**F**) Left and middle panels show that, after transduction with Ad-p90RSK-WT or Ad-GFP as a control for 12 hours, MLECs were assayed and quantified for apoptosis by FITC annexin V staining (left) and for telomere lengths (middle). Data represent mean ± SD, $n = 6$. Right panel shows that MLECs were transfected with the NF-κB reporter gene for 24 hours, followed by transduction with Ad-p90RSK WT or Ad-GFP as a control for 12 hours. NF-κB activity was assayed using the dual-luciferase reporter assay. Data represent mean ± SD, $n = 6$, $^{**}P < 0.01$. All statistical analyses in this figure were done by 1-way ANOVA followed by Bonferroni post hoc test.

that targeted TERF2IP deletion in stratified epithelial tissue led to shorter TLs in skin cells (13). Therefore, it is possible that the total TERF2IP depletion in *Terf2ip*^{homo}-EKO/*Ldlr* cannot completely inhibit d-flow–induced TL shortening and subsequent apoptosis, which is mediated by nuclear TRF2.

Discussion

In this study, we found that TERF2IP has a crucial role in concurrently regulating EC activation and senescence. Our findings suggest that phosphorylation of TERF2IP at S205 provokes nuclear export of TERF2IP, which is accompanied by TRF2. The association of extranuclear TERF2IP increases NF-κB activation to induce EC activation. Furthermore, the cotransport into the cytoplasm of TERF2IP with TRF2 removes the latter from the nucleus, thereby promoting TL shortening, senescence, and subsequent apoptosis. Thus, inflammatory signaling and TL shortening are coupled through this mechanism, providing a new explanation for the linkage between the SASP and TL shortening (35). In addition, we found that the depletion of endothelial TERF2IP inhibited d-flow–induced plaque formation in mice. Together, these data suggest that TERF2IP simultaneously regulates EC activation, apoptosis, and senescence and exacerbates plaque formation.

It has been suggested that TL shortening is not involved in atherosclerosis but, rather, that short TLs inhibit atherosclerosis (36). This idea is based on the results of 2 separate papers that reported that proinflammatory stress and atherosclerosis caused increased TERT expression (37) and reduced atherosclerosis lesion formation in RNA component of telomerase, TERC-apoE–double-KO mice, although the TL length was shorter in these mice than in control mice (38). However, these experimental results could be interpreted in a different way. Nontelomeric roles for telomerase — including activation of transcription factor E2F (39) as a transcriptional modulator, which increases cell proliferation — have been well established (7, 40–42). In addition, the absence of TERC abolishes the proliferative effect of TERT overexpression (43, 44). Therefore, it is possible that the inhibition of atherosclerosis in TERC-KO mice is due to the systemic effect of telomerase on cell proliferation. As mentioned above, TERT can directly associate with p65 and increase NF-κB activity and inflammation, which also play significant roles in promoting atherogenesis. Thus, the contribution of TL length to atherosclerotic plaque formation cannot be rejected by the data obtained from telomerase-KO mice because the depletion of telomerase can also inhibit both proliferation and EC activation. In the current study, we found that TERF2IP coordinately regulated EC senescence and activation and the depletion of endothelial TERF2IP significantly reduced d-flow–induced atherosclerosis, supporting the role of EC senescence and activation in atherosclerosis. Further studies are necessary to specifically clarify the role of EC senescence and activation in atherosclerosis.

The crucial role of TERF2IP in regulating lipopolysaccharide- or TNF-α–induced cytokine production in THP-1 cells has been reported by Cai et al. (25). However, these authors found no effects of TERF2IP on proinflammatory gene expression in HUVECs and MLECs induced by LPS, TNF-α, and IL-1β. We found that, under the unstimulated condition, TERF2IP was mainly localized in the nucleus, but after stimulation by d-flow or TNF-α, TERF2IP was exported from the nucleus to the cytosol, and this cytosolic TERF2IP had proinflammatory effects. In contrast, Cai et al. show significant cytosolic expression of TERF2IP levels in unstimulated cells, suggesting that additional TERF2IP nuclear export might not have a significant impact under their experimental condition, and they were unable to detect a significant effect of cytoplasmic TERF2IP.

The role of NF-κB activation in regulating TERF2IP expression has been reported (20). Since d-flow increases and l-flow decreases NF-κB activation, it is very reasonable that we found a higher expression level

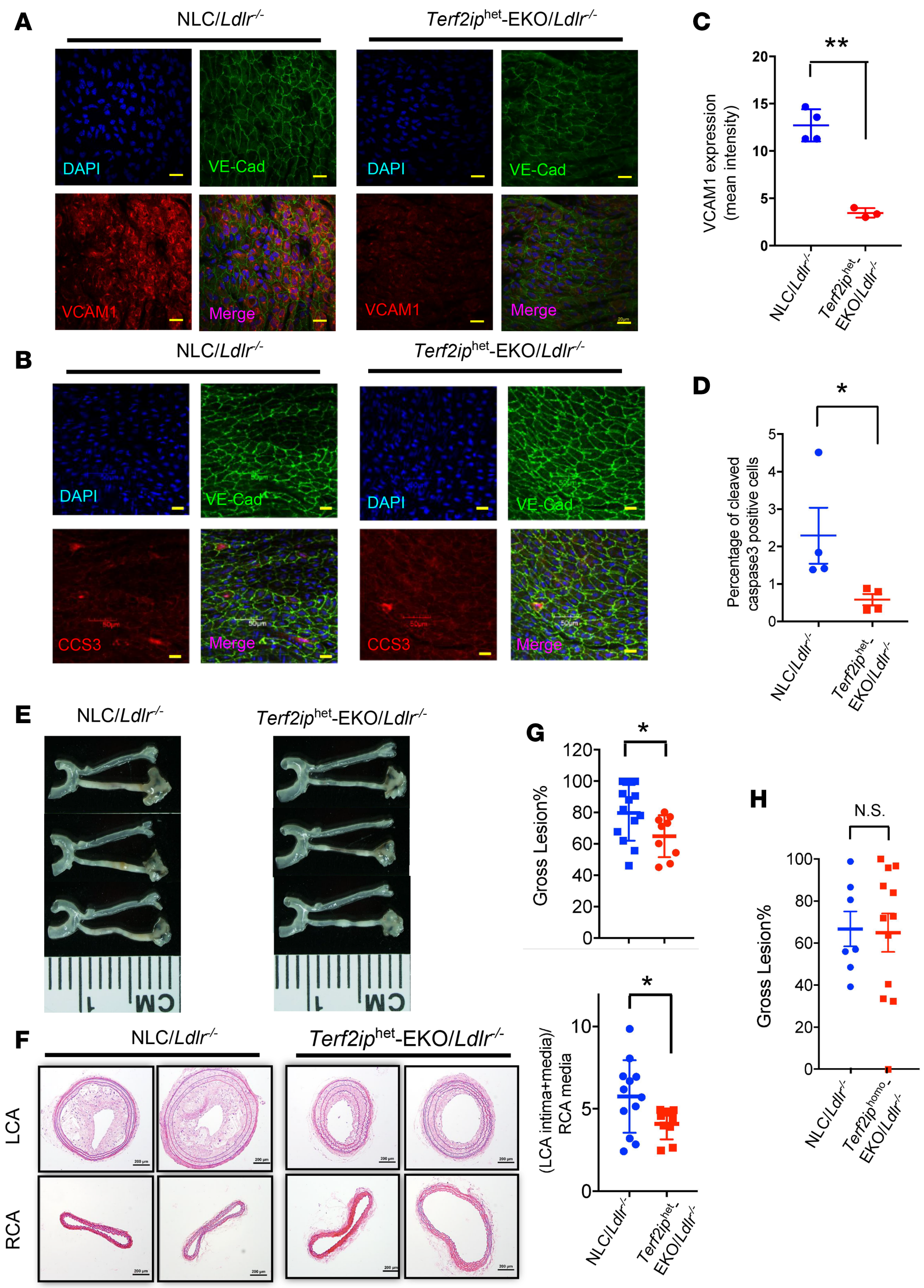

Figure 9. Endothelial activation and apoptosis, as well as subsequent atherosclerosis formation, were decreased in *Terf2ip*^{het}-EKO/*Ldlr* mice in vivo. (**A** and **B**) En face preparations of mouse aortas were coimmunostained with antibodies against vascular endothelial–cadherin (VE-Cad) and VCAM-1 (**A**) or cleaved caspase 3 (CCS3) (**B**). Fluorescent images of VCAM-1 and CCS3 expression in areas exposed to d-flow were recorded using an Olympus confocal laser scanning microscope (FV1200 MPE) with a 60× objective lens (NA 1.35na Oil) (left). Scale bars: 20 μm. (**C** and **D**) The histogram shows the reduced intensity of anti–VCAM-1 (**C**) and anti-CC3 (**D**) staining in the d-flow region of the *Terf2ip*^{het}-EKO/*Ldlr* mice. Data are presented as mean ± SD ($n = 4$/group), $^{**}P < 0.01$, $^{*}P < 0.05$ by unpaired 2-tailed t test. (**E**–**H**) Mice were fed a high-fat diet for 2 weeks, and PLCL surgery was performed. Four weeks after the surgery, the gross plaque size (plaque length/total left carotid length) in the *Terf2ip*^{het}-EKO/*Ldlr* mice (**E** and **G**, top) and in the *Terf2ip*^{homo}-EKO/*Ldlr* mice (**H**) were measured. Data are shown as mean ± SD, $n = 9$–12, $^{*}P < 0.05$ by unpaired 2-tailed t test. (**F**) Representative images of H&E-stained sections of the left carotid artery (LCA) and right carotid artery (RCA), obtained from *Ldlr* or *Terf2ip*^{het}-EKO/*Ldlr* mice after 4 weeks of partial LCA ligation. After ligation, neointima formation in the LCA of WT mice occurred, which was inhibited in *Terf2ip*^{het}-EKO/*Ldlr* mice. Scale bars: 200 μm. (**G**, bottom) The LCA plaque size (intima + media)/RCA media ratios in H&E-stained LCA and RCA sections were calculated as described in the Methods. Data are presented as mean ± SD, $n = 9$–12, $^{*}P < 0.05$ by unpaired 2-tailed t test.

of TERF2IP expression in the d-flow area than in the l-flow area. In our in vitro study, we did not observe a significance difference in TERF2IP expression between d-flow and static conditions, potentially because the increase of TERF2IP expression by d-flow–induced NF-κB activation could be canceled by the effect of TERF2IP degradation after nuclear export, which is relevant to the condition after TRF2 depletion (Figure 7C). In contrast, in vivo, we compared TERF2IP expression between d-flow and l-flow areas. Therefore, the increase of TERF2IP expression induced by d-flow via increasing NF-κB activation and the decrease of TERF2IP expression induced by l-flow via inhibiting NF-κB activation may become more apparent than the comparisons in d-flow vs. static conditions in vitro. We will investigate this possibility in our future study.

We could not exclude the indirect effect of apoptotic genomic DNA degradation on TL shortening. However, although the depletion of TERF2IP almost completely inhibited d-flow–induced TL shortening, depletion of TERF2IP partially inhibited the γ-H2AX increase induced by d-flow, suggesting a direct effect of TERF2IP on TL shortening that is independent of apoptotic genomic DNA degradation.

In summary, we provide evidence that TERF2IP S205 phosphorylation promotes the nuclear export of the TERF2IP-TRF2 complex. This, in turn, leads to a proinflammatory and prosenescence phenotype in ECs, which contributes to atherosclerotic plaque formation. Future studies are necessary to determine how nuclear export of TERF2IP TRF2 contributes to the regulation of a distinct gene set that causes EC activation and senescence.

Methods

Additional details of the experimental procedures are included in the online Supplemental Methods.

Mice and left carotid artery partial ligation. Mice were maintained in the vivaria of the Texas A&M Institute of Bioscience and Technology and The University of Texas MD Anderson Cancer Center. All animals were housed in a temperature-controlled room under a light (12-hour)/dark (12-hour) cycle and pathogen-free conditions. EC-specific TERF2IP-KO mice were generated using mice expressing *Cre*-recombinase under the regulation of VE-cadherin promoter (C57BL/6 background), as described previously (28). These mice were crossed with B6;129-*Terf2ip*$^{\mathrm{tm1.1Tdl}}$/J mice (stock no. 012346; The Jackson Laboratory). Genotyping of pups was performed by PCR using a tail clipping. DNA was extracted with a Zymo kit (Zymo Research) as per product protocol, and PCR was performed with GoTaq Green Master Mix (Promega) as per product protocol. To confirm the TERF2IP-null condition, we isolated ECs from homozygous mice and determined the KO effect on EC senescence and inflammation in vitro.

To show the functional role of endothelial TERF2IP in vivo, we used heterozygous mice. To our knowledge, total knockdown of TERF2IP expression does not exist in nature; therefore, heterozygous mice should exhibit more physiological in vivo responses than homozygous mice. Animals were challenged with a high-fat diet (TD.88137, Envigo) for 2 weeks, and then partial left carotid artery ligation was performed. In brief, 3 of the 4 caudal branches of the left carotid artery (left external carotid, internal carotid, and superior thyroid artery) were ligated with a 6–0 silk suture, while the occipital artery was left intact (45).

Monitoring of mice after surgery. After surgery, mice were monitored until recovery in a chamber on a heating pad. We injected postoperative analgesia as needed for additional pain relief. We supported the mice with (a) warmth by placing them in a prewarmed cage (on a heating pad) and (b) fluids (prewarmed normal saline [37°C, 5 ml per 100 g body weight], given s.c.). We checked on the mice every 10 minutes until they were awake and moving, then daily for the first 3 days, and then once per week until the conclusion of the study, as described in our protocols.

Histologic type and evaluation of atherosclerotic lesions after partial carotid ligation. Four weeks after surgery, the left and the right carotid arteries of the mice were harvested, fixed, paraffin embedded, serially sectioned (5 μm), and stained with H&E, as we described previously (22). Plaque formation was evaluated by detecting the intima and media areas and quantifying them using ImageJ software (http://imagej.nih.gov/ij/), as we described previously (22). The intima area was calculated by subtracting the lumen area from the area circumscribed by the internal elastic lamina, and the media area was determined by the area between the internal and external elastic laminae. We conducted a double-blind, randomized study; the researchers who evaluated the sizes of plaques were blinded to the study groups until the data analysis was complete.

Real-time PCR. At the end of experiments, ECs were washed 3 times with PBS and lysed in RLT Plus RNeasy lysis buffer (74136; QIAGEN). The resulting cell lysates were loaded onto a QIAshredder column (79656; QIAGEN) and spun down to collect the eluted lysates. Total RNA was then isolated from this lysate using an RNeasy Plus Mini Kit (74136; QIAGEN) following the manufacturer's instructions. cDNA reverse transcription was performed with a 50 μl reaction mixture containing 1 μg of purified RNA, 5 μl of 10× buffer, 11 μl of $MgCl_2$, 10 μl of dNTPs, 2.5 μl of a random hexamer, 1.25 μl of oligo-dT, 1 μl of RNase inhibitor, and 0.75 μl of a reverse transcriptase enzyme using TaqMan Reverse Transcription Reagents (N808-0234; made for Applied Biosystems by Roche Molecular Diagnostics). First-strand cDNA was reverse transcribed from total RNA by incubating reaction mixtures at 25°C for 10 minutes followed by 37°C for 60 minutes, 42°C for 60 minutes, and 95°C for 5 minutes before soaking at 4°C in a

PCR cycler. Target cDNA levels were quantified using a CFX Connect Real-Time System (Bio-Rad). Each reaction mixture (10 μl) contained cDNA synthesized from 20 ng of total RNA, 5 μl of iQ SYBR Green Supermix (1708882; Bio-Rad), and 0.5 μmol/l each of forward and reverse primer, purchased from Origene with qSTAR quantitative PCR (qPCR) primers shown in Supplemental Table 2). Real-time PCR was carried out using MyiQTM2 Two-Color Real Time PCR System (Bio-Rad) and SYBR Green (Bio-Rad) at thermal activation for 10 minutes at 95°C and 40 cycles of PCR (melting for 15 seconds at 95°C, followed by annealing/extension for 1 minute at 60°C). The ΔΔCt method was used to calculate fold changes in expression of target RNAs: ΔCt = Ct (target gene) – Ct (housekeeping gene, GAPDH); ΔΔCt = ΔCt (treatment) – ΔCt (control); and fold change = $2^{(-\Delta\Delta Ct)}$.

TUNEL assay. Cell apoptosis was measured using the TUNEL assay (Roche Diagnostics). HUVECs were exposed to d-flow for 24 hours and fixed with 4% paraformaldehyde. After fixation, cells were washed with PBS, chilled in an ice bath for 2 minutes with permeabilization solution, washed again with PBS, and incubated with a TUNEL mixture of terminal deoxynucleotidyl transferase and dUTP in DNA-labeling solution for 1 hour at 37°C. Cells were then rinsed twice with PBS and incubated with 50 μl of enzyme-labeled anti-fluorescein antibody solution in the dark for another 30 minutes. After the cells had been rinsed with PBS, 3,3-diaminobenzidine was added for color development, and H&E was used for counterstaining. For each experimental group, a total of 400 cells from 5 high-power field images was examined under a microscope.

Flow cytometric analysis of apoptotic cells for determining EC purity. Following various treatments (as indicated in the figures), cells were washed 3 times with PBS and harvested using 10 mM EDTA (pH 8.0) solution at room temperature, and stained for apoptotic marker annexin V using annexin V–FITC Apoptosis Detection Reagent (ab14082; Abcam) as per the manufacturer's instructions. Briefly, cell pellets were resuspended in 1× annexin V Binding Buffer, and baseline measurements were taken using unstained control cells. Then, cells were stained with annexin V–FITC (ab14083; Abcam) at room temperature for 5 minutes in the dark. For detecting EC purity, cells were stained with FITC conjugated anti–mouse CD31 (102405; BioLegend). Measurements for all samples were carried out using an Accuri C6 flow cytometer (BD Biosciences). Ten thousand cells were counted based on forward and side scatter characteristics. Results were analyzed using FlowJo software (version 10.5.0, FlowJo LLC).

TL length assay. TL length was measured using the TL PNA kit with FITC (DAKO), per the manufacturer's instructions. In brief, cells were suspended in PBS and heated to 82°C for 10 minutes, either in the hybridization solution containing the fluorescein-conjugated PNA TL probe or in the hybridization solution without the probe. Hybridization was allowed to proceed in the dark at room temperature overnight. Cells were then washed twice, for 10 minutes each, using the washing solution supplied with the kit at 40°C. Cells were resuspended in the DNA staining buffer and incubated for 1 hour at room temperature. After being washed, cells were analyzed with a BD Accuri C6 flow cytometer using the FL-1 channel to detect the FITC signal and the FL-3 channel for propidium iodide. We used the human 1301 cell line (T-cell leukemia, 01151619-1VL, MilliporeSigma) as a control cell line because these cells have unusually long TLs. These cells were cultured in RPMI 1640 containing 2 mM L-glutamine and 10% FBS, and the TL signal was measured as described above. After the flow cytometric analysis, the data obtained were used to determine the relative TL length, and the relative TL length was calculated as the ratio between the TL signal of each sample and the control cell (1301 cell line), with correction for the DNA index of G0/1 cells.

NF-κB activity assay. NF-κB activity was measured using a luciferase assay with a reporter gene containing 5 NF-κB binding sites as an enhancer (pLuc-MCS with 5 repeated NF-κB binding sites [TGGGGACTTTCCGC]; Stratagene). A transfection mixture was made using GIBCO Opti-MEM Reduced Serum Medium (31985070; Thermo Fisher Scientific) to which DEAE-DEXTRAN (final concentration, 0.375 μg/μl, D9885; MilliporeSigma), a reporter vector, and a pRL-CMV vector (Promega) were added, and the mixture was incubated for 10 minutes at 37°C. pRL-CMV was used as an internal control for Renilla luciferase activity. Next, culture medium was removed, cells were washed with PBS, and the transfection mixture was added. After 90 minutes of incubation, cold Opti-MEM Reduced Serum Medium containing 5% DMSO was added to the cells, and the mixture was incubated for an additional 5 minutes. Cells were then washed once with PBS and cultured in normal extracellular matrix (ECM). At the completion of experiments, cells were harvested in a passive lysis buffer (E1960; Promega), and the NF-κB activity was determined by using a GloMax 20/20 Luminometer (Promega) to measure luciferase activity in resulting cell lysates (dual-luciferase reporter assay system; E1960, Promega). Relative NF-κB activity was calculated by normalizing firefly luciferase activity to Renilla luciferase activity (firefly/Renilla luciferase activity ratio).

Gene expression profiling. Total RNA was obtained using RNeasy columns (QIAGEN) with DNA digest, according to the manufacturer's instructions, and hybridized to Affymetrix GeneChip Human Transcriptome Array 2.0 (Affymetrix). The array data were incorporated into the Transcriptome Analysis Console 3.0 software program (Affymetrix); GeneChip data were normalized using Tukey's biweight average algorithm and represented as a biweight average on a $\log_2$ scale. Significant differences between 2 groups were identified using an unpaired ANOVA ($P < 0.05$) with $\log_2$-transformed normalized intensities, and transcripts with more than 2-fold differences in expression and $P < 0.05$ were selected for each specific comparison analyzed. Data were analyzed using Ingenuity Pathway Analysis application build 377306M (2016-03-16) and content version 27216297 (2016-03-16; QIAGEN). We identified statistically significant and activation states of (a) canonical pathways, (b) biological functions and disease, and (c) predicted upstream transcriptional regulators (http://pages.ingenuity.com/rs/ingenuity/images/0812%20downstream_effects_analysis_whitepaper.pdf) using Fisher's exact test enrichment scoring and predicated activity states with z-score calculations, which were based on the correlation between gene expression changes and literature-substantiated gene effects. Interaction networks were based on gene or molecule connectivity with other genes and molecules in the analyzed dataset (46). All molecular interactions and relationships of molecules to function or disease were based on curated findings in the literature, which are stored in the Ingenuity Knowledge Base (QIAGEN).

Data availability. The microarray data are available in a public repository from the NCBI website under the GEO accession number GSE119407. The authors declare that all of the other data supporting the findings of this study are available in the article, in the supplemental material, or from the corresponding author upon request.

Statistics. Data are presented as the mean ± SD. Differences between 2 independent groups were determined using the Student *t* test (2-tailed) and, when applicable, 1-way ANOVA, followed by Bonferroni post hoc testing for multiple group comparisons using Prism software (version 5.0; GraphPad Software). When groups exhibited unequal variances, Welch's ANOVA was used to perform multiple group comparisons. $P < 0.05$ were considered statistically significant and are indicated by an asterisk in the figures. $P < 0.01$ are indicated by 2 asterisks.

Study approval. All animal and human cells procedures were approved by the University Committee on Animal Resources of the Texas A&M Institute of Bioscience and Technology (2014-0231, 2017-0154) and by the MD Anderson IACUC (00001652, 00001109) and the MD Anderson IRB (PA17-0383).

Author contributions

SK, HTV, KAK, YW, MI, KSH, YF, TNT, YJG, HM, JPM, JHS, YT, JLMM, and NTL generated animals, performed experiments, and analyzed data. SK, KF, NTL, and JA conceived and designed the experiments. CJG generated TERF2IP constructs. KAK, KSH, SK, and TNT performed the animal experiments. KF, SK, NTL, and JA wrote the manuscript. JPC made suggestions for the study design and experiments. JT provided FMK-MEA and commented on the study design. AJL provided HAECs and made suggestions for the study design and experiments. All authors commented on the manuscript.

Acknowledgments

We thank the Department of Scientific Publications at The University of Texas MD Anderson for proofreading the article. This work was supported by the NIH/National Cancer Institute under award number P30CA016672 (used the Sequencing and Microarray Facility) and by funding from the NIH to JA (HL130193, HL123346, and HL118462), NTL (HL134740), and JPC (HL133254).

Address correspondence to: Jun-ichi Abe, University of Texas MD Anderson Cancer Center, 2121 West Holcombe Boulevard, IBT8.803E, Unit 1101, Houston, Texas 77030, USA. Phone: 713.745.2803; Email: jabe@mdanderson.org. Or to: Nhat-Tu Le, Houston Methodist Research Institute, 6670 Bertner Avenue, R10-216 MS: R10 South, Houston, Texas 77930, USA. Phone: 713.363.8080; Email: Nhle@houstonmethodist.org. Or to: Keigi Fujiwara, University of Texas MD Anderson Cancer Center, 2121 West Holcombe Boulevard, IBT8.805, Unit 1101, Houston, Texas 77030, USA. Phone: 713.745.8262; Email: kfujiwara1@mdanderson.org.

KSH's present address is: Institute of Drug Research & Development, Chungnam National University, Daejeon, Republic of Korea.

YF's present address is: Department of Radiology-Research, Houston Methodist Research Institute, Houston Texas, USA.

JHS's present address is: Department of Gastroenterology Hepatology & Nutrition, The University of Texas MD Anderson Cancer Center, Houston, Texas, USA.

1. Gimbrone MA, García-Cardeña G. Endothelial Cell Dysfunction and the Pathobiology of Atherosclerosis. *Circ Res*. 2016;118(4):620–636.
2. Erusalimsky JD. Vascular endothelial senescence: from mechanisms to pathophysiology. *J Appl Physiol*. 2009;106(1):326–332.
3. Minamino T, Komuro I. Vascular cell senescence: contribution to atherosclerosis. *Circ Res*. 2007;100(1):15–26.
4. Salpea KD, et al. Association of telomere length with type 2 diabetes, oxidative stress and UCP2 gene variation. *Atherosclerosis*. 2010;209(1):42–50.
5. Mortuza R, Chen S, Feng B, Sen S, Chakrabarti S. High glucose induced alteration of SIRTs in endothelial cells causes rapid aging in a p300 and FOXO regulated pathway. *PLoS ONE*. 2013;8(1):e54514.
6. Collins C, Tzima E. Hemodynamic forces in endothelial dysfunction and vascular aging. *Exp Gerontol*. 2011;46(2-3):185–188.
7. Martínez P, Blasco MA. Telomeric and extra-telomeric roles for telomerase and the telomere-binding proteins. *Nat Rev Cancer*. 2011;11(3):161–176.
8. de Lange T. Shelterin: the protein complex that shapes and safeguards human telomeres. *Genes Dev*. 2005;19(18):2100–2110.
9. Ogami M, et al. Telomere shortening in human coronary artery diseases. *Arterioscler Thromb Vasc Biol*. 2004;24(3):546–550.
10. Samani NJ, Boultby R, Butler R, Thompson JR, Goodall AH. Telomere shortening in atherosclerosis. *Lancet*. 2001;358(9280):472–473.
11. Li B, Oestreich S, de Lange T. Identification of human Rap1: implications for telomere evolution. *Cell*. 2000;101(5):471–483.
12. Sfeir A, Kabir S, van Overbeek M, Celli GB, de Lange T. Loss of Rap1 induces telomere recombination in the absence of NHEJ or a DNA damage signal. *Science*. 2010;327(5973):1657–1661.
13. Martinez P, et al. Mammalian Rap1 controls telomere function and gene expression through binding to telomeric and extratelomeric sites. *Nat Cell Biol*. 2010;12(8):768–780.
14. Kabir S, Sfeir A, de Lange T. Taking apart Rap1: an adaptor protein with telomeric and non-telomeric functions. *Cell Cycle*. 2010;9(20):4061–4067.
15. de Lange T. How telomeres solve the end-protection problem. *Science*. 2009;326(5955):948–952.
16. Dunham MA, Neumann AA, Fasching CL, Reddel RR. Telomere maintenance by recombination in human cells. *Nat Genet*. 2000;26(4):447–450.
17. Celli GB, Denchi EL, de Lange T. Ku70 stimulates fusion of dysfunctional telomeres yet protects chromosome ends from homologous recombination. *Nat Cell Biol*. 2006;8(8):885–890.
18. Celli GB, de Lange T. DNA processing is not required for ATM-mediated telomere damage response after TRF2 deletion. *Nat Cell Biol*. 2005;7(7):712–718.
19. Platt JM, et al. Rap1 relocalization contributes to the chromatin-mediated gene expression profile and pace of cell senescence. *Genes Dev*. 2013;27(12):1406–1420.
20. Teo H, et al. Telomere-independent Rap1 is an IKK adaptor and regulates NF-kappaB-dependent gene expression. *Nat Cell Biol*. 2010;12(8):758–767.
21. Takai KK, Hooper S, Blackwood S, Gandhi R, de Lange T. In vivo stoichiometry of shelterin components. *J Biol Chem*. 2010;285(2):1457–1467.
22. Heo KS, et al. Disturbed flow-activated p90RSK kinase accelerates atherosclerosis by inhibiting SENP2 function. *J Clin Invest*. 2015;125(3):1299–1310.
23. Chen Y, et al. A conserved motif within RAP1 has diversified roles in telomere protection and regulation in different organisms. *Nat Struct Mol Biol*. 2011;18(2):213–221.
24. Coluzzi E, et al. Transient ALT activation protects human primary cells from chromosome instability induced by low chronic oxidative stress. *Sci Rep*. 2017;7:43309.
25. Cai Y, et al. Rap1 induces cytokine production in pro-inflammatory macrophages through NFκB signaling and is highly expressed in human atherosclerotic lesions. *Cell Cycle*. 2015;14(22):3580–3592.
26. Li B, de Lange T. Rap1 affects the length and heterogeneity of human telomeres. *Mol Biol Cell*. 2003;14(12):5060–5068.
27. Xue Y, Ren J, Gao X, Jin C, Wen L, Yao X. GPS 2.0, a tool to predict kinase-specific phosphorylation sites in hierarchy. *Mol Cell Proteomics*. 2008;7(9):1598–1608.
28. Le NT, et al. A crucial role for p90RSK-mediated reduction of ERK5 transcriptional activity in endothelial dysfunction and atherosclerosis. *Circulation*. 2013;127(4):486–499.
29. Kfoury Y, et al. Ubiquitylated Tax targets and binds the IKK signalosome at the centrosome. *Oncogene*. 2008;27(12):1665–1676.
30. Rai R, Chen Y, Lei M, Chang S. TRF2-RAP1 is required to protect telomeres from engaging in homologous recombination-mediated deletions and fusions. *Nat Commun*. 2016;7:10881.
31. van Steensel B, Smogorzewska A, de Lange T. TRF2 protects human telomeres from end-to-end fusions. *Cell*. 1998;92(3):401–413.
32. Dunn J, et al. Flow-dependent epigenetic DNA methylation regulates endothelial gene expression and atherosclerosis. *J Clin Invest*. 2014;124(7):3187–3199.

33. Nam D, et al. Partial carotid ligation is a model of acutely induced disturbed flow, leading to rapid endothelial dysfunction and atherosclerosis. *Am J Physiol Heart Circ Physiol*. 2009;297(4):H1535–H1543.
34. Merino H, Parthasarathy S, Singla DK. Partial ligation-induced carotid artery occlusion induces leukocyte recruitment and lipid accumulation--a shear stress model of atherosclerosis. *Mol Cell Biochem*. 2013;372(1-2):267–273.
35. Liu Y, Bloom SI, Donato AJ. The role of senescence, telomere dysfunction and shelterin in vascular aging. *Microcirculation*. 2019;26(2):e12487.
36. Goodman WA, Jain MK. Length does not matter: a new take on telomerase reverse transcriptase. *Arterioscler Thromb Vasc Biol*. 2011;31(2):235–236.
37. Gizard F, et al. Telomerase activation in atherosclerosis and induction of telomerase reverse transcriptase expression by inflammatory stimuli in macrophages. *Arterioscler Thromb Vasc Biol*. 2011;31(2):245–252.
38. Poch E, Carbonell P, Franco S, Díez-Juan A, Blasco MA, Andrés V. Short telomeres protect from diet-induced atherosclerosis in apolipoprotein E-null mice. *FASEB J*. 2004;18(2):418–420.
39. Xiang H, Wang J, Mao Y, Liu M, Reddy VN, Li DW. Human telomerase accelerates growth of lens epithelial cells through regulation of the genes mediating RB/E2F pathway. *Oncogene*. 2002;21(23):3784–3791.
40. Saretzki G. Extra-telomeric functions of human telomerase: cancer, mitochondria and oxidative stress. *Curr Pharm Des*. 2014;20(41):6386–6403.
41. Saretzki G. Telomerase, mitochondria and oxidative stress. *Exp Gerontol*. 2009;44(8):485–492.
42. Chiodi I, Mondello C. Telomere-independent functions of telomerase in nuclei, cytoplasm, and mitochondria. *Front Oncol*. 2012;2:133.
43. Cayuela ML, Flores JM, Blasco MA. The telomerase RNA component Terc is required for the tumour-promoting effects of Tert overexpression. *EMBO Rep*. 2005;6(3):268–274.
44. Flores I, Cayuela ML, Blasco MA. Effects of telomerase and telomere length on epidermal stem cell behavior. *Science*. 2005;309(5738):1253–1256.
45. Ko KA, Fujiwara K, Krishnan S, Abe JI. En face preparation of mouse blood vessels. *J Vis Exp*. 2017;(123):e55460.
46. Krämer A, Green J, Pollard J, Tugendreich S. Causal analysis approaches in Ingenuity Pathway Analysis. *Bioinformatics*. 2014;30(4):523–530.